1. General

Inconel Alloy MA 6000 (MA 6000), an advanced nickel-base alloy produced by mechanical alloying, exhibits exceptional mechanical properties over a broad temperature range. It is the oxide-dispersion-strengthened (ODS) counterpart of the superalloy IN-738. MA 6000 combines solution strengthening by tungsten and molybdenum, precipitate strengthening by coherent gamma-prime Ni_3Al, and dispersion strengthening by yttria. Precipitate hardening enhances strength at intermediate temperatures, in the range of 1400F, while dispersion hardening, combined with a large, elongated grain structure is effective at 2000F and higher. The high temperature strength capabilities of MA 6000 are generally superior to those exhibited by single crystal alloys. High temperature creep rupture properties are not degraded by thermal cycling or long-time stressed exposure beyond the extent attributable to normal coarsening of the gamma-prime phase. The alloy has good high- and low-cycle fatigue resistance and thermal fatigue resistance. Oxidation resistance is imparted by aluminum and chromium, while aluminum, titanium, tantalum, chromium, and tungsten contribute to sulfidation resistance. Coatings are frequently employed to further improve the high temperature oxidation/corrosion resistance. MA 6000 is thermo-mechanically processed and annealed to produce a coarse, highly elongated grain structure which is critical to the development of high strength at high temperatures. The grain aspect ratio (GAR) is typically greater than 10:1. MA 6000 was developed primarily as an airfoil material for use in advanced gas turbine engines. It is also finding application in land-based gas turbine engines (Refs. 1-7).

1.1 Commercial Designation

Inconel Alloy MA 6000.

1.2 Alternate Designations

Inconel MA 6000, MA 6000.

1.3 Specifications

1.4 Composition

1.4.1 *[Table]* Nominal composition.

1.5 Heat Treatment

Standard heat treatment consists of zone annealing to produce the large, elongated grain structure necessary for high temperature strength, followed by solution annealing and double aging to dissolve and reprecipitate the gamma-prime phase. The zone anneal consists of passing the workpiece through a controlled-atmosphere high-frequency furnace at 1 to 12 in./hr at a temperature of 2250 to 2350F. The gamma-prime heat treatment consists of solution annealing at 2250F, 0.5 hr, air cool, plus double aging at 1750F, 2 hr, air cool, plus 1550F, 24 hr, air cool (Some references in this report did not report the metallurgical condition of the starting material. For those citations where processing information is either absent or indicated to be unavailable, it is assumed that the material was processed according to the standard heat treatment.) (Refs. 1, 4, 8).

Ni

15 Cr

4.0 W

2.0 Mo

4.5 Al

2.5 Ti

2.0 Ta

1.1 Y_2O_3

The development of a large-grained structure is critical in the fabrication of mechanically alloyed materials such as MA 6000 in order to obtain the desired high temperature mechanical strength in the final product.

In the extruded plus hot-rolled condition, MA 6000 is fine-grained with an average grain diameter of approximately 0.2 micron. The dislocation density is low, indicating that primary recrystallization occurs during fabrication. On annealing below the gamma-prime solvus temperature (about 2120F), hot worked material exhibits normal grain growth characteristics. However, this fine-grained microstructure is unsuitable for high temperature service because of low strength properties (Ref. 9).

The required highly elongated, large-grained microstructure is achieved by zone annealing of hot-worked material. The sharp temperature gradient in the hot zone promotes exaggerated grain growth through secondary recrystallization, with the maximum zone temperature held in the rather narrow range above the gamma-prime solvus and below the liquidus temperature (2365F). The desired microstructure is achieved when the rate of travel of the material through the hot zone is equal to or less than the rate of grain boundary movement at the maximum hot zone temperature. This condition suppresses the nucleation of new grains and promotes growth of existing grains (Ref. 10). At higher speeds, grain nucleation occurs in preference to grain growth and the resulting microstructure is equiaxed rather than elongated. The transition from elongated to equiaxed macrograins occurs at higher material travel speeds as the peak temperature in the annealing zone is increased (Ref. 11). During secondary recrystallization, the transformation to a large columnar grained structure occurs rapidly, with grain size increasing by four orders of magnitude within two to five minutes. The large grains resulting from zone annealing are elongated in the direction of travel through the hot zone, which is usually the direction of primary working. This directionally recrystallized microstructure is largely a result of annealing in a temperature gradient with only a minor contribution from anisotropic grain growth associated with non-uniform distribution of grain-boundary-pinning oxide particles (Refs. 12, 13).

The effects of annealing temperature on grain size of warm extruded, fine grained alloy are shown in Figure 1.5.1. Although these data were obtained by isothermal annealing, the same principles apply to zone annealing with regard to temperature. There is a well-defined minimum temperature near the gamma-prime solvus temperature which must be exceeded for secondary recrystallization to occur, with the largest grain sizes being observed after annealing just above this temperature. The grain sizes decrease with further increases in temperature, reflecting an increase in grain boundary unpinning rates relative to grain growth rates. This behavior, typical for secondary recrystallization, is in contrast to the increase in grain size with increasing annealing temperature usually observed during primary recrystallization. It is noteworthy that the grain aspect ratios obtained during isothermal annealing do not exceed about two, whereas ratios of ten and higher are obtainable by zone annealing under appropriate conditions. The onset of secondary recrystallization with increasing annealing temperature is accompanied by a sharp drop in hardness, shown in Figure 1.6.1.

Additional warm prestraining of the hot-worked starting material affects both the grain size and the grain aspect ratio obtained after subsequent zone annealing, as shown in Figure 1.5.2. At strains up to about 0.8, little effect is observed and the desirable large grain sizes and high aspect ratios are achieved. However, for prestrains of about 1.4, the subsequent grain size and grain aspect ratio are considerably reduced. This behavior is attributed to a reduction in the driving force for secondary recrystallization caused by increased amounts of primary recrystallization with increasing prestrain (Ref. 14).

Directional recrystallization of extruded material gives a <110> texture along the longitudinal axis. This is attributed to the lower energy of <110> tilt boundaries (Ref. 15). This texture is less desirable than a <100> texture from the standpoint of thermal fatigue resistance and intermediate temperature creep strength (Refs. 10, 16).

1.5.1 *[Figure]* Effects of annealing temperature on grain size and grain aspect ratio.

1.5.2 *[Figure]* Effects of prestraining on grain size and grain aspect ratio after zone annealing.

1.6 Hardness

1.6.1 *[Figure]* Effect of annealing temperature on hardness.

1.7 Forms and Conditions Available

Bar and small forgings (Ref. 17).

1.8 Melting and Casting Practice

MA 6000 is consolidated by mechanical alloying. This process was developed during the 1970's and reached commercial status during the 1980's. It is essentially a method for producing composite metal powders with a controlled microstructure from elements which are normally difficult or impossible to combine by conventional melting techniques. In the case of MA 6000, mechanical alloying allows the incorporation of fine, insoluble yttria particles into a gamma-prime strengthened superalloy matrix. The process consists essentially of repeated fracturing and rewelding of a mixture of powder particles, at least one of which must be ductile, in a dry, high energy ball mill operated at or slightly above room temperature. Industrial ball mills for mechanical alloying are of large diameter and are rotated at high speed. During each collision of the grinding balls, many powder particles are trapped and plastically deformed. Sufficient deformation occurs to rupture any absorbed surface contaminant film and expose clean metal surface. Cold welds are formed where metal particles overlay, producing composite metal particles. At the same time, other work-hardened particles are fractured. The cold welding, which tends to increase the size of the particles involved, and the fracturing, which tends to reduce particle size, reach a steady state balance leading ultimately to a relatively coarse but stable overall particle size. These competing processes of cold welding and fracture occur repeatedly throughout the milling, gradually kneading the particles so that their structure is continually refined and homogenized. The particles become microcomposites, with the composition of each particle converging to that of the starting blend (Refs. 13, 17-19).

Mechanical alloying should be distinguished from conventional ball milling, which is simply mixing on a fine scale. Monitoring of the mechanical alloying process by x-ray diffraction has confirmed that true alloying occurs. This alloying results from interdiffusion of the constituents caused by heating from the kinetic energy of the balls during mechanical alloying and the very small diffusion distances associated with fine mixing of the constituents (Refs. 10, 18).

A typical starting powder mixture for MA 6000 consists of fine (4-7 micron) nickel powder, 75-150 micron chromium, minus 45 micron molybdenum and tantalum, minus 11 micron tungsten, and minus 150 micron nickel-base master alloys containing aluminum, titanium, boron, and zirconium. About 2.5 volume percent of very fine yttria (250 to 400 angstroms) is also added to form the dispersoid. After completion of the powder milling a uniform interparticle spacing of about 0.5 micron is achieved. At this point the dispersoid has reacted with aluminum in the matrix to form a mixed oxide of Y_2O_3-Al_2O_3 (Refs. 10, 20).

The highly cold-worked state of mechanically alloyed powders precludes cold pressing, requiring consolidation by a combination of high temperature and pressure. Usual commercial practice includes simultaneous consolidation and primary fabrication by encapsulating the mechanically alloyed powder charge in a mild steel can and extruding to bar at 1850 to 1950F at an extrusion ratio of about 13:1. Other methods which have been used with some success include: hot compaction followed by hot extrusion; and hot isostatic pressing (Refs. 4, 18, 19).

1.9 Special Considerations

1.9.1 High temperature strength properties are critically dependent on the attainment of a large, highly elongated grain structure. This structure is developed, first, by close control of thermomechanical processing steps to assure the retention of adequate work in the microstructure. Secondly, the properly worked material must be zone annealed under correct conditions of maximum temperature and rate of passage of the workpiece through the hot zone. Good strength at intermediate temperatures and exceptional strength at high temperatures are attainable in properly processed material (See Sections 1.5, 3.3, 3.4, and 4.1).

1.9.2 Long time mechanical properties are anisotropic because of the highly oriented grain structure. Although short term tensile properties are little affected, longer term creep rupture strengths are higher in the longitudinal than in the transverse direction. The directionality of strength properties increases with increasing temperature (See Sections 3.3 and 3.4).

1.9.3 MA 6000 has good oxidation resistance to temperatures of about 2000F, but protective coatings are needed for long time service at higher temperatures in oxidizing environments (See Section 2.3.4).

1.9.4 Special care is required in joining. Best joint strengths are obtained by diffusion welding using isostatic pressing or hot pressing techniques. Brazing is suitable for use at temperatures to 1800F. Fusion welds are subject to cracking and agglomeration of dispersoids (See Section 4.3).

2. Physical Properties and Environmental Effects

2.1 Thermal Properties

2.1.1 Melting Range: 2365-2507F (Ref. 1).

2.1.2 Phase Changes.

2.1.2.1 Time-temperature-transformation diagrams. Although the dispersoid initially added to the MA 6000 powder mix is yttrium oxide, Y_2O_3, the particles in extruded MA 6000 actually consist of mixed Al-Y oxides. These mixed oxides are: yttrium aluminum garnet, $Y_3Al_5O_{12}$ (YAG); yttrium aluminum perovskite, $YAlO_3$ (YAP); yttrium aluminum monoclinic, $Y_4Al_2O_9$ (YAM); and yttrium aluminum hexagonal, $YAlO_3$ (YAH). These compounds also contain up to 13 percent zirconium metal ions randomly substituted for yttrium and aluminum metal ions in the oxide lattice. The dispersoid in hot rolled material is similar to that in extruded material, both consisting of about 50 percent YAH phase and the remainder being YAG, YAP, and YAM phases in roughly equal proportions. However, after zone annealing, the YAM phase is no longer present. In this condition, the YAH phase constitutes about 90 percent of the dispersoid, and the YAG and YAP phases are present in about equal amounts (Ref. 21).

The average particle diameter increases from about 170 angstroms in the hot rolled material to about 230 angstroms after zone annealing. Very little oxide coarsening occurs during exposure at 1382 to 1400F, but significant growth is observed at 1742 to 2012F, as shown in Figure 2.1.2.1.1. Coarsening is thought to follow a parabolic relationship. This type of time dependency would indicate that an interface reaction is rate-controlling, such as transfer of atoms across the precipitate/matrix interface (Ref. 21).

It is not yet clear whether the increase in dispersoid diameter is due to dissolution of small dispersoids ("Ostwald ripening") or to interaction of yttria particles with aluminum dissolved in the matrix. The former would increase the average dispersoid spacing and thereby degrade the strength of the alloy, but the latter would not. Available data suggest that the composition of the mixed yttria-alumnia dispersoid can change during high temperature exposure, favoring the latter reaction (Ref. 10).

Coarser particles are occasionally found in the microstructure. These particles have been identified as titanium carbonitrides and aluminum oxide and are present in the form of stringers aligned parallel to the extrusion direction (Ref. 10).

The gamma-prime phase, which constitutes about 50 percent of the structure, exhibits a duplex size distribution; the majority of this phase is present as blocky particles of similar size as the matrix grains with the remainder present as a fine dispersion (Ref 9). The gamma-prime phase loses coherency with the matrix and coarsens rapidly at 1800F, as shown in Figure 2.1.2.1.2 (Refs. 5, 22).

The gamma-prime solvus temperature is about 2120F (Ref. 4).

2.1.2.1.1 *[Figure]* Effects of exposure time on yttria dispersoid particle size at 1382 to 2012F.

2.1.2.1.2 *[Figure]* Effects of exposure time on gamma-prime particle size at 1400 to 1800F.

2.1.3 Thermal Conductivity.

2.1.3.1 *[Figure]* Thermal conductivity.

2.1.4 Thermal Expansion.

2.1.4.1 *[Figure]* Mean coefficient of linear thermal expansion.

2.1.5 Specific Heat.

2.1.5.1 *[Figure]* Specific heat.

2.1.6 Thermal Diffusivity.

2.2 Other Physical Properties

2.2.1 Density: 0.293 lb/cu in., 8.11 g/cc (Ref. 1, p. 2).

2.2.2 Electrical Properties.

2.2.3 Magnetic Properties.

2.2.4 Emittance.

2.2.5 Damping Capacity.

2.3 Chemical Environments

2.3.1 General Corrosion. MA 6000 has good resistance to corrosion in a wide variety of environments (Ref. 7).

2.3.2 Stress Corrosion.

2.3.3 Hydrogen Effects.

2.3.4 Oxidation. MA 6000 has excellent oxidation resistance in air and can be used in the uncoated condition in vane applications in gas turbine aircraft engines at temperatures up to 2012F. As shown in Figure 2.3.4.1, exposure at 1832F results in slight weight gains, indicating the formation of a protective scale. Some flaking occurs at 2012F, giving weight losses. Minimal internal attack occurs at these temperatures. However, significant metal losses are observed at 2192F, and additional protection is needed for continuous service at this temperature. MA 6000 forms an alpha-alumina-rich scale (Ref. 23). The cyclic oxidation resistance of uncoated MA 6000 in air at 2012F is superior to that of IN-713LC and IN-738 but less than that of IN-100, as shown in Table 2.3.4.2.

Overlay coatings such as applied by plasma spraying or physical vapor deposition are promising for oxidation protection at high temperatures (Ref. 24).

Uncoated MA 6000 performs well in burner rig testing. At 1700F, the oxidation/corrosion resistance of MA 6000 is superior to that of IN-100 and IN-713LC, but less than that of IN-738, MA 956, and MA 754, as shown in Figure 2.3.4.3 and Table 2.3.4.4. Additional data, shown in Table 2.3.4.5, indicate that MA 6000 is comparable to both MA 754 and Mar-M 509 at 1700F but superior at 2000F. Although a protective alumina scale forms at the surface, internal sulfidation is observed in uncoated MA 6000 to a depth of 2 mils after rig testing at 1700F and to a depth of 3 mils after testing at 2000F for 312 hours (included in "Maximum Attack" data, Table 2.3.4.5). A plasma-sprayed nickel-base coating protected MA 6000 from oxidation and sulfidation for 312 hours at both 1700 and 2000F, but developed some interfacial voiding after rig testing for 500 hours at 2000F. A second nickel-base underlayer provided additional protection from oxidation and sulfidation for 500 hours at 2000F and eliminated interfacial void formation (Refs. 7, 23, 25, 26).

A NiCoCrAlY coating is used commercially to extend the life of first-stage MA 6000 turbine blades in a stationary gas-turbine engine to 25,000 design service hours at a turbine inlet temperature of 2075F (Ref. 6).

The resistance to ignition by friction in oxygen is an important consideration in some aerospace applications. The data in Table 2.3.4.6 indicate the MA 6000 has intermediate resistance to frictional ignition in comparison with a number of other aerospace alloys. This listing also indicates that resistance to frictional ignition generally increases with increasing nickel content (Ref. 27).

2.3.4.1 *[Figure]* Oxidation weight change behavior in air at elevated temperatures.

2.3.4.2 *[Table]* Cyclic oxidation resistance at 2012F of MA 6000 compared with three other superalloys.

2.3.4.3 *[Figure]* Metal loss and maximum attack after burner rig testing for 500 hours at 1700F for MA 6000 and three other superalloys.

2.3.4.4 *[Table]* Burner rig oxidation resistance at 1700F of MA 6000 and three other superalloys.

2.3.4.5 *[Table]* Burner rig oxidation resistance at 1700 and 2000F.

2.3.4.6 *[Table]* Frictional ignition of MA 6000 and other aerospace alloys.

2.4 Nuclear Environments

3. Mechanical Properties

3.1 Specified Mechanical Properties

3.2 Mechanical Properties at Room Temperature

3.2.1 Tension Stress-Strain Diagrams and Tensile Properties.

3.2.2 Compression Stress-Strain Diagrams and Compression Properties.

3.2.3 Impact.

3.2.4 Bending.

3.2.5 Torsion and Shear.

3.2.6 Bearing.

3.2.7 Stress Concentration.

3.2.7.1 Notch properties.

3.2.7.1.1 *[Table]* Effects of notches on room temperature tensile properties in helium and in hydrogen.

3.2.7.2 Fracture toughness.

3.2.8 Combined Loading.

3.3 Mechanical Properties at Various Temperatures

3.3.1 Tension Stress-Strain Diagrams and Tensile Properties. Representative stress-strain diagrams for coarse- and fine-grained materials are shown in Figures 3.3.1.1 and 3.3.1.2, respectively (See also Figure 3.5.2.4).

Large-grained MA 6000 exhibits slightly higher tensile strength in the longitudinal than in the transverse direction, as shown in Figures 3.3.1.3 and 3.3.1.4. Low ductilities are observed at all temperatures in the transverse direction but longitudinal material shows a modest increase in ductility at temperatures greater than 1400F.

Tensile strength varies with imposed strain rate in an equivalent manner to the variation of creep rate with imposed creep stress, as shown in Figure 3.3.1.5. Here, the tensile strength is defined as the maximum true stress during tensile deformation and the creep rate is that observed during steady state creep. The similarity in behavior over several orders of magnitude variation in deformation rates indicates similarity in deformation mechanisms in both creep and tensile at equivalent deformation rates (Ref. 29).

A decrease in tensile strength with decreasing strain rate is also shown by the data in Figure 3.3.1.6. Material fabricated by a combination of extrusion and hot rolling is slightly stronger than material fabricated only by extrusion. No clear trend is apparent with regard to material orientation (Ref. 28).

In the as-rolled, fine-grained condition, MA 6000, like other mechanically alloyed materials, is considerably weaker than in the standard, large-grained condition. This is seen by comparison of flow stresses for the fine-grained material in Figure 3.3.1.7 with creep stresses for coarse-grained alloy at similar deformation rates, shown later in Figures 3.4.6 and 3.4.9. MA 6000 is considered superplastic, exhibiting an elongation of 308 percent and a strain rate sensitivity of 0.47 at 1832F, as shown in Figure 3.3.1.8. The deformation process of fine-grained MA 6000 is described as a combination of power law creep and diffusional (Coble) creep, with threshold stress caused by the presence of gamma-prime particles affecting only the diffusional creep process. Intricately shaped parts of MA 6000 can be hot-formed in the fine-grained condition and subsequently annealed to obtain the coarse-grained creep-resistant structure (Ref. 30).

3.3.1.1 *[Figure]* Effect of strain rate on tensile stress-strain diagrams for coarse-grained alloy at 1400F.

3.3.1.2 *[Figure]* Tensile stress-strain diagram for fine-grained alloy at 2012F.

3.3.1.3 *[Figure]* Effects of temperature on longitudinal tensile properties of annealed bar.

3.3.1.4 *[Figure]* Effects of temperature on transverse tensile properties of annealed bar.

3.3.1.5 *[Figure]* Variation of strength with strain rate or creep rate at 1400F.

3.3.1.6 *[Figure]* Effects of strain rate, orientation, and fabrication method on tensile strength at 1400F.

3.3.1.7 *[Figure]* Effects of strain rate and temperature on flow stress of fine grained alloy.

3.3.1.8 *[Figure]* Effects of strain rate on tensile strain rate sensitivity and ductility for fine-grained alloy at 1832F.

3.3.2 Compression Stress-Strain Diagrams and Compression Properties. Compressive stress-strain diagrams from room temperature to 2192F are shown in Figure 3.3.2.1. At low temperatures, ductility is low and fracture occurs after only slight amounts of work hardening. At 1472F and above, ductility is higher and deformation proceeds at a fairly constant flow stress (Ref. 31).

MA 6000 has high compressive yield strength which exhibits only slight temperature dependency up to about 1300F. Above this temperature, the yield strength decreases strongly with increasing temperature, as shown in Figure 3.3.2.2. The steady state flow data at 1562F, shown in Figure 3.3.2.3, follow the creep (flow) equation:

$$\dot{e} = K\sigma^n$$

where $\dot{e}$ = steady creep (or flow) rate

σ = applied stress

n = observed stress exponent

K = proportionality constant

The observed stress exponent approximates 13.6 in the linear region of these data, compared to usual values of 3 to 5 for particle-free alloys. This high value for the stress exponent suggests that the observed high strength of MA 6000 includes substantial contributions from the dispersoid and the gamma-prime phase. The strength increments due to the yttria dispersoid and the gamma-prime second phase are estimated from these data as 30 to 44 ksi and 36 to 49 ksi, respectively, at 1562F (Ref. 31).

The effects of orientation on compressive steady state flow behavior at 1600 to 2000F are shown in Figure 3.3.2.4. The short transverse orientation is slightly stronger than the longitudinal or long transverse, in contrast to tensile behavior where the transverse orientation is slightly weaker than longitudinal. This difference between tensile and compressive flow strengths is attributed to the inability of grain boundaries to support high tensile stresses, leading to tensile failures which originate at the grain boundaries. Under high temperature compressive conditions, failure occurs by concentrated slip along several crystallographic planes of the large grained material (Ref. 32).

3.3.2.1 *[Figure]* Compressive stress-strain diagrams at room temperature to 2192F.

3.3.2.2 *[Figure]* Effects of temperature on compressive 0.2-percent yield strength.

3.3.2.3 *[Figure]* Effects of strain rate on compressive steady state flow stress at 1562F.

3.3.2.4 *[Figure]* Effects of orientation and temperature on compressive steady state flow stress.

3.3.3 Impact.

3.3.4 Bending.

3.3.5 Torsion and Shear. The shear strength at 1400F is 41.4 ksi in tension (average of three tests) and 99.0 ksi in compression (average of two tests) (Ref. 33).

3.3.6 Bearing.

3.3.7 Stress Concentration.

3.3.7.1 Notch properties.

3.3.7.2 Fracture toughness.

3.3.8 Combined Loading.

3.4 Creep and Creep Rupture Properties

Several creep strengthening concepts are successfully incorporated in MA 6000. At intermediate temperatures, creep strength is controlled by the high volume fraction of gamma-prime precipitate with only a small strength contribution from the yttria dispersion. However, at higher temperatures, the creep strength is derived primarily from the inert oxide dispersion.

The creep strength of MA 6000 is compared to those of conventional and single crystal superalloys in Figure 3.4.1. MA 6000 is stronger than the single crystal alloy at high temperatures and low stresses but weaker at intermediate temperatures and high stresses. The lesser strength of MA 6000 at intermediated temperatures reflects the fact that it is not possible to obtain the same gamma-prime strengthening in columnar grains as in single crystals (Ref. 16).

Creep and rupture data from several sources are summarized in Figures 3.4.2, 3.4.3, and 3.4.4 and Table 3.4.5. The alloy is weaker in the transverse direction that in the longitudinal direction, especially at higher temperatures, as seen by comparison of the data in Figures 3.4.3 and 3.4.4. Fracture is transgranular and crystallographic cracking is observed. The elongation to failure is low and decreases with increasing temperature (Ref. 34).

Steady creep rates and rupture lives for heat treated, large grained material at 1400 and 2000F are shown in Figures 3.4.6 and 3.4.7, respectively. The observed stress dependence n of steady creep (see flow equation in Paragraph 3.3.2) is high for MA 6000 (and other ODS alloys), varying in the present data from 24 at 1400F to 48 at 2000F. This unusual creep behavior has been rationalized by describing the stress dependence of the creep rate in terms of an effective stress rather than simply in terms of the applied stress. The effective stress is the applied stress minus a temperature-dependent threshold stress related to pinning of dislocation by second phase (gamma-prime or yttria) particles. This behavior reflects particle and precipitate strengthening in addition to solution strengthening of the matrix (Ref. 34).

The grain aspect ratio (GAR) is influential in determining the high temperature creep strength of MA 6000, as shown by the data in Figure 3.4.8. A GAR of 20 or above is needed to take full advantage of dispersion strengthening. Above this minimum GAR, long rupture lives are observed and the fracture mode is transgranular. However, as the GAR decreases to below 10, the creep fracture mode changes to intergranular and rupture lives are dramatically decreased. The deterioration of creep life and change from transgranular to intergranular fracture with decreasing GAR are caused by the growth of creep cavities on transverse grain boundaries. The higher frequency of these boundaries in low-GAR material leads to shorter rupture life. It is further noted that creep failure even in high-GAR material usually initiates in fine-grained "defect" regions, which have a higher proportion of transverse grain boundaries, emphasizing the creep-deleterious nature of transverse grain boundaries (Refs. 35, 36).

Another important result of the vulnerability of transverse grain boundaries is the pronounced anisotropy of tensile creep properties. While short-term tensile and compressive strength are relatively insensitive to loading direction with respect to the extrusion axis, tensile creep strength is substantially reduced in the transverse direction, as noted above and shown in Figure 3.4.9. The reason is again the occurrence of premature intergranular fracture at the longitudinal grain boundaries, with an accompanying severe reduction in ductility. Compressive strength in the long transverse direction is greater than that of long transverse tensile but less than that of longitudinal tensile, particularly at low creep rates. It has been suggested that tensile and compressive weakness in the long transverse direction may result from diffusional creep at stresses below the threshold stress for dislocation creep in the longitudinal direction (Refs. 37, 38).

The shear rupture strength of MA 6000 at 1400F approximates 0.45 of the tensile rupture strength, as shown in Figure 3.4.10. Shear failure surfaces are relatively brittle, with very little indication of ductile accommodation (Ref. 39).

Crack growth rates under static load are clearly affected by orientation at 1832F, as shown in Figure 3.4.11. In the T-L orientation, the growth rate increases normally with increasing stress intensity. However, in the L-T orientation, secondary cracking alters the crack growth behavior and the growth rate decreases with increasing stress intensity. This anomalous rate reduction of the primary crack is due to the development of perpendicular secondary cracks along planes of aligned coarse particle stringers (Ref. 40).

The creep rate at 1400F is substantially reduced under cyclic creep conditions as compared to creep under static conditions. This behavior is shown in Figure 3.4.12 as the ratio of net cyclic creep rate (based on time under load) to the static creep rate under the same maximum load as a function of frequency. The reduced cyclic creep strength is attributed to partial recovery of creep strain and of the accompanying backstress during the off-load period, resulting in an increase in the effective stress as a fraction of the applied stress (Ref. 41).

3.4.1 *[Figure]* Effects of temperature on 100-hour rupture strength of MA 6000, MA 754, and three non-ODS superalloys.

3.4.2 *[Figure]* Creep rupture behavior at 1292 to 2100F.

3.4.3 *[Figure]* Longitudinal creep rupture behavior of annealed bar at 1300 to 2100F.

3.4.4 *[Figure]* Transverse creep rupture behavior of annealed bar at 1400 to 2000F.

3.4.5 *[Table]* Creep rupture properties of annealed bar at 1400 and 2000F.

3.4.6 *[Figure]* Creep rate behavior of annealed bar at 1400 and 2000F.

3.4.7 *[Figure]* Rupture life behavior of annealed bar at 1400 and 2000F.

3.4.8 *[Figure]* Effects of grain aspect ratio on rupture life at 1742F and 33.4 ksi.

3.4.9 *[Figure]* Effects of orientation on tensile and compressive creep rate behavior at 1922F.

3.4.10 *[Figure]* Shear and tensile creep rupture behavior.

3.4.11 *[Figure]* Effect of orientation on creep crack growth rates in vacuum at 1832F.

3.4.12 *[Figure]* Effects of load cycling on creep rate of annealed bar at 1400F and maximum stress of 77 ksi.

3.5 Fatigue Properties

3.5.1 Conventional High-Cycle Fatigue. The high-cycle fatigue behavior of MA 6000 is shown in Figure 3.5.1.1. MA 6000 has very good high-cycle fatigue strength, higher than those of other conventional wrought or cast superalloys. The high-cycle fatigue resistance of MA 6000 is also superior to that of its non-ODS counterpart IN-738 (Ref. 3). Additionally, the endurance ratio (ratio of fatigue strength at 10^7 cycles to ultimate tensile strength) at ambient temperature is high at 0.52. Typical values for endurance ratios for conventional superalloys range from 0.2 to 0.4. High-cycle fatigue failure occurs by transgranular crack propagation, similar to the behavior exhibited during low-cycle fatigue (Ref. 42).

The high-cycle fatigue strength of longitudinal specimens is significantly greater than that of transverse specimens at 1562F, as shown in Figure 3.5.1.2. Fatigue fractures initiate at inclusion defects and propagate transgranularly for both specimen orientations. The fracture surfaces are smooth for longitudinal specimens. In contrast, fracture surfaces for transverse specimens contain rough regions which reflect crack branching along grain boundaries (Ref. 43).

3.5.1.1 *[Figure]* High-Cycle fatigue behavior at room and elevated temperatures.

3.5.1.2 *[Figure]* Effect of orientation on high-cycle fatigue behavior at 1562F.

3.5.2 Low-Cycle Fatigue. Cyclic stress-strain curves exhibit the expected softening with increasing temperature and with decreasing strain rate, as shown in Figures 3.5.1.1 and 3.5.1.2. In comparison with monotonic stress-strain curves, the cyclic curves are slightly softer at low strains and slightly harder at higher strains, shown in Figure 3.5.2.3 (Refs. 44, 45).

The low-cycle fatigue resistance at room temperature and 1400F is the same for lives less than about 10^3 cycles, as shown in Figure 3.5.2.4. For lives greater than this, the room temperature fatigue resistance appears to be somewhat greater than that at 1400F. Fatigue fracture occurs in a transgranular mode at both temperatures. At room temperature, the individual fatigue curves (not shown) exhibit an initial period of cyclic strain hardening, followed by strain softening. In contrast, only strain softening is observed during fatigue at 1400F (Ref. 42).

Increasing temperature above 1400F results in generally decreasing low-cycle fatigue life, as shown in Figure 3.5.2.5. This behavior is particularly apparent at lower strain amplitudes and longer fatigue lives. At 1562F, decreasing the imposed strain rate from $1x10^{-2}$ sec^{-1} to $2x10^{-5}$ sec^{-1} has little effect on fatigue life, as shown in Figure 3.5.2.6. However, at 1922F, this same reduction in strain rate results in a considerable decrease in fatigue life, probably associated with the increasing microstructural degradation from processes such as creep or oxidation. Fatigue fracture is transgranular at 1562F but becomes mixed with intergranular/transgranular at 1922F (Refs. 44, 46).

In air, the resistance to low-cycle fatigue decreases with increasing temperature, as noted above and shown in Figure 3.5.2.7. However, in vacuum at the same temperatures, the fatigue resistance is slightly greater than that in air and does not decrease with increasing temperature, shown in Figure 3.5.2.8. The deleterious effect of air on fatigue resistance is attributed to oxidation (Ref 47).

Failure under creep-fatigue loading conditions occurs more rapidly than under pure fatigue loading conditions. This is shown in Figure 3.5.2.9, where the failure life at 1562F under slow-fast loading (tension strain rate $1x10^{-5}$ sec^{-1}/compression strain rate $1x10^{-2}$ sec^{-1}) is shorter than that under symmetrical fast-fast loading (strain rate $1x10^{-2}$ sec^{-1}) by a factor of about 10. Somewhat less damaging are the slow-slow cycle (strain rate $1x10^{-5}$ sec^{-1}) with a factor of 5 reduction and the tensile-hold cycle, with a factor of 4 reduction. The slow-fast fatigue lives at 1922F are also considerably shorter than those at 1562F. Unsymmetrical loading is thought to affect fatigue behavior by accelerating or inhibiting diffusional growth of grain boundary cavities which subsequently coalesce and lead to crack initiation. Creep cavities in MA 6000 nucleate primarily at recrystallization defects in the form of pockets of small grains, which comprise about 5 percent of the total volume. These cavities grow by stress-directed diffusion of vacancies from the grain boundaries to the void surfaces (Refs. 48, 49).

The life of MA 6000 under low-cycle fatigue and creep-fatigue conditions is comparable to that exhibited by its non-ODS counterpart IN-738. The lack of improvement in MA 6000 may be attributed to the increasing effect of time-dependent damage with decreasing loading frequency, to which grain structure defects in ODS alloys are particularly susceptible (Ref. 3).

3.5.2.1 *[Figure]* Effect of temperature on cyclic stress-strain curves at 1400 to 1922F.

3.5.2.2 *[Figure]* Effects of strain rate on cyclic stress-strain curves at 1562 and 1922F.

3.5.2.3 *[Figure]* Cyclic and monotonic stress-strain curves at 1562 to 1922F.

3.5.2.4 *[Figure]* Low-cycle fatigue behavior at room temperature and 1400F.

3.5.2.5 *[Figure]* Effect of temperature on low-cycle fatigue behavior at 1400 to 1922F.

3.5.2.6 *[Figure]* Effects of strain rate on low-cycle fatigue behavior at 1562 and 1922F.

3.5.2.7 *[Figure]* Low-cycle fatigue behavior at elevated temperatures in air.

3.5.2.8 *[Figure]* Low-cycle fatigue behavior at elevated temperatures in vacuum.

3.5.2.9 *[Figure]* Effects of strain rate and loading asymmetry on low-cycle fatigue behavior at 1562 and 1922F.

3.5.3 Fatigue Crack Propagation. The fatigue crack growth rates generally increase with increasing temperature, as shown in Figures 3.5.3.1 to 3.5.3.3. However, the scatter in data is such that some observed high temperature rates are about equal to or less than rates at lower temperatures. Frequency and stress intensity factor range may also affect the temperature dependency of crack growth rates. At room temperature, the fatigue cracks propagate by crystallographic shearing of gamma-prime, but at higher temperatures the mechanism changes. At 1562F, cracks are highly sensitive to microstructural inhomogeniety, with subsidiary grain boundary cracking associated with the oxidation of the agglomerated gamma-prime phase (Refs. 50-52).

Fatigue crack growth rates tend to increase with decreasing frequency, but the effect is less strong than that of temperature and is sometimes obscured by data scatter. At 1202F, the crack propagation rates exhibit a slight increase with decreasing frequency, as shown in Figure 3.5.3.4. Mixed trends are observed at 1562F, as shown in Figures 3.5.3.5 and 3.5.3.6. However, a clear trend of increasing crack growth rate with decreasing frequency is seen in the T-L orientation at 1652F, Figure 3.5.3.7. The frequency effect of crack propagation may result from the retarding effect of crack branching along grain boundaries at low frequencies (Refs. 2, 50, 51).

Although fatigue crack propagation behavior in MA 6000 is considered to be orientation-dependent, the nature of this dependence is inconsistent and may in turn be influenced by one or more other factors, such as frequency and/or crack branching. At room temperature and 1562F, crack propagation transversely to the extrusion direction (L-T orientation) is faster then parallel to the extrusion direction (T-L orientation), as shown in Figures 3.5.3.8 and 3.5.3.9. The difference in rates for the two orientations is greatest at low delta-K values, with the rates tending to converge as delta-K increases to greater than 20 ksi (in.)$^{0.5}$ (Refs. 43, 50). However, at a much lower frequency (0.17 Hz versus 10 or 40 Hz), opposite behavior occurs, as shown in Figure 3.5.3.10. Here, the crack growth rates are higher for the T-L orientation than for the L-T orientation (Ref. 40). Aside from possibly the lower frequency, the reason for this difference is not obvious. It is suggested that caution be exercised in drawing conclusions regarding orientation effects on fatigue crack growth rates.

The crack propagation rates in vacuum are greater than those in air at 1562F at frequencies of 0.01 and 10 Hz, as shown in Figure 3.5.3.11. This behavior is attributed to oxide blocking effects which can lead to a reduction in the effective delta-K at the crack tip, thus reducing the crack growth rates in air (Ref. 53).

3.5.3.1 *[Figure]* Effect of temperature on fatigue crack growth rates at room temperature to 1562F.

3.5.3.2 *[Figure]* Effect of temperature on fatigue crack growth rates at room temperature to 1742F.

3.5.3.3 *[Figure]* Effect of temperature on fatigue crack growth rates at room temperature and 1832F.

3.5.3.4 *[Figure]* Effect of frequency on fatigue crack growth rates at 1202F.

3.5.3.5 *[Figure]* Effect of frequency on fatigue crack growth rates at 1562F using compact tension specimens.

3.5.3.6 *[Figure]* Effect of frequency on fatigue crack growth rates at 1562F using edge notch tensile specimens.

3.5.3.7 *[Figure]* Effects of temperature and frequency on fatigue crack growth rates.

3.5.3.8 *[Figure]* Effect of specimen orientation on fatigue crack growth rates at room temperature.

3.5.3.9 *[Figure]* Effect of specimen orientation on fatigue crack growth rates at 1562F.

3.5.3.10 *[Figure]* Effects of temperature and orientation on fatigue crack growth rates.

3.5.3.11 *[Figure]* Effects of environment and two different frequencies on fatigue crack growth rates at 1562F.

3.5.4 Thermal Fatigue. MA 6000 has excellent thermal fatigue resistance as compared to other nickel-base and cobalt-base alloys, as shown in Table 3.5.4.1. Cycles to first crack are over 10,000 for both bare and coated MA 6000. Typically, conventionally cast superalloys crack within 500 cycles, while several thousand cycles are required before cracks initiate in directionally solidified alloys (Ref. 42).

3.5.4.1 *[Table]* Thermal fatigue behavior of MA 6000 compared with several other superalloys.

3.6 Elastic Properties

3.6.1 Poisson's Ratio.

3.6.2 Modulus of Elasticity.

3.6.2.1 *[Figure]* Modulus of elasticity.

3.6.3 Modulus of Rigidity.

3.6.4 Tangent Modulus.

3.6.5 Secant Modulus.

4. Fabrication

4.1 Forming

Extrusion of mechanically alloyed powder is conducted at 1850 to 1950F, with recrystallization occurring during extrusion to produce a fine equiaxed grain structure. Hot rolling is performed in the same temperature range with the extrusion can in place in order to minimize cracking. Hot rolling at 1850F tends to cause edge cracking, but not at temperatures above 1875F. Reductions of about 20 percent per pass are employed with total thickness reductions ranging up to 90 percent (Refs. 4, 54). Precise control of the overall thermomechanical working sequence, including total rolling reduction, rolling temperature, and speed and number of passes, is necessary so that the optimum amount of stored mechanical energy is retained in the material for subsequent directional recrystallization during zone annealing. A minimum thickness reduction of 40 to 60 percent is required to produce the exaggerated grain growth response (Refs. 4, 7, 20).

MA 6000 cannot be forged in the recrystallized condition because of its low ductility but hot working in the fine-grained as-extruded condition is possible. Careful control of the forging conditions is necessary to avoid cracking which tends to occur at lower strain rates and loss of driving force for recrystallization which occurs at higher deformation rates (Refs. 10, 55).

Both isothermal and conventional forging are attractive for MA 6000. Isothermal forging, which combines preheating of dies and workpiece to the same temperature with low deformation rates, utilizes superplasticity to produce near-net-shape blades with minimum material input. The conventional forging approach is less expensive but uses more material, gives oversize forgings, and has less control over shape due to the presence of the thermal barrier layer which is required to prevent chilling (Refs. 5, 56). The preferred forging route is dependent on the size and complexity of the final product. Conventional forging is likely more applicable to small pieces, while the more expensive isothermal process may be more advantageous costwise for larger pieces (Refs. 5, 20, 57).

Care must be exercised during conventional hot forging because of the die chilling problem. An adherent cladding, either the original extrusion can or a thick plating, is required to prevent cracking of the workpiece. The temperature range in order to produce the proper grain structure after recrystallization is 1850 to 1950F, with 1900F being optimum. Deformation levels up to 70 percent do not adversely affect subsequent recrystallization. However, sharp transitions in tooling designs should be avoided because of the potential for introducing grain structure discontinuities in the workpiece. Elevated temperature stress-rupture properties of forged blades are somewhat degraded as compared to those for standard hot-rolled bar, as shown in Figure 4.1.1 (Ref. 58).

4.1.1 *[Figure]* Effects of temperature and orientation on rupture life at several locations on forged and annealed blade and comparison with annealed bar.

4.2 Machining and Grinding

MA 6000 can be machined readily by conventional procedures for high nickel alloys. The machineability of MA 6000 is similar to that of Udimet 700 and better than that of IN-713 and IN-738. The alloy should be machined in the recrystallized condition (Ref. 7). MA 6000 is also amenable to electrical-discharge (EDM) and electrochemical machining (ECM) (Refs. 6, 8, 10).

4.3 Joining

MA 6000 is similar to other dispersion-strengthened materials in that fusion joining methods cause agglomeration of the dispersoids and consequent reduction of stress-rupture strength. MA 6000 also tends to crack during fusion welding (Refs. 7, 8).

MA 6000 can be readily brazed using nickel- and cobalt-based brazing alloys (Refs. 10, 59). MA 6000 joined by vacuum brazing with B93 braze alloy (Ni-14Cr-9.5Co-4.5Si-4W-4Mo-3Al-0.7B), for example, is suitable for service at temperatures up to 1800F. Since the brazing temperature for this braze alloy (2200F) is near the solution heat treatment temperature (2250F), brazing should be followed by double aging (1750F, 2 hr, AC plus 1550F, 24 hr, AC) to ensure good high temperature strength (Ref. 8).

MA 6000 can be joined most successfully by hot press or hot isostatic press diffusion welding.

The hot press method consists of pressing the faying surfaces together in vacuum at 1832 or 2192F for 1.25 hours. Best joints are produced when unrecrystallized fine grained material is joined to similar material. Joints between recrystallized and unrecrystallized material produced joints with lower rupture strengths, as shown in Figure 4.3.1. It is considered that plastic flow during hot pressing is required to produce the strongest joints. This is possible when using unrecrystallized alloy because of its low strength and relatively good ductility at high temperatures. However, the high strength and limited ductility of zone recrystallized material tend to cause cracking when stresses high enough to produce flow are applied by hot pressing. When diffusion welding is conducted in the unrecrystallized condition, welding must be followed by the usual double age heat treatment (Refs. 10, 60).

Hot-isostatic-pressing (HIP) can also be employed to produce sound diffusion welded joints in MA 6000. Although details of the HIP procedure are not available, it is reported advantageous as compared to uniaxial hot pressing because pressures exceeding the compressive yield strength can be employed without causing cracking. Good joints can be made by HIP welding with recrystallized as well as unrecrystallized alloy. The short-time tensile strength of HIP-welded joints is comparable to that of commercial recrystallized alloy up to 1742F, as shown in Figure 4.3.2. However, the longer time rupture strengths are less than those of the base alloy, similar to the relationship shown for hot-press diffusion welded joints above in Figure 4.3.2 (Ref. 61).

4.3.1 *[Figure]* Effects of recrystallization and welding parameters on rupture strength of hot press diffusion welded joints at 1832F.

4.3.2 *[Figure]* Tensile strength of hot-isostatic-press diffusion welded joints at room and elevated temperatures.

4.4 Surface Treating

Table 1.4.1 Nominal composition (Ref. 1)

Alloy	MA 6000
Component	**Percent**
Chromium	15
Tungsten	4.0
Molybdenum	2.0
Aluminum	4.5
Titanium	2.5
Tantalum	2.0
Carbon	0.05
Boron	0.01
Zirconium	0.15
Yttrium Oxide (Y_2O_3)	1.1
Nickel	balance

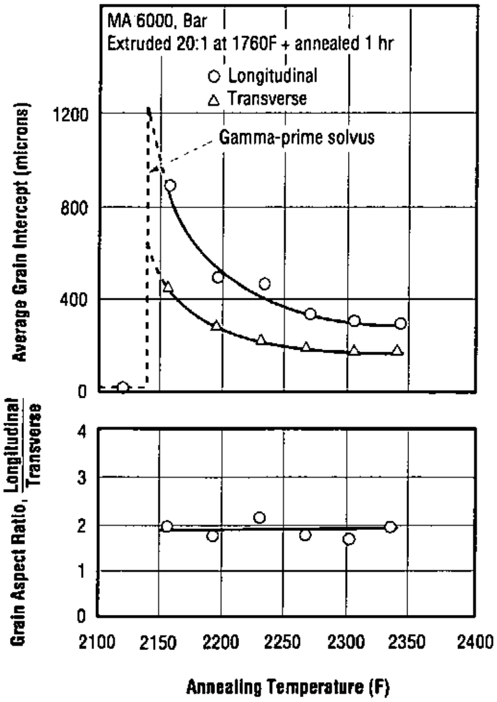

Fig. 1.5.1 Effects of annealing temperature on grain size and grain aspect ratio (Ref. 14)

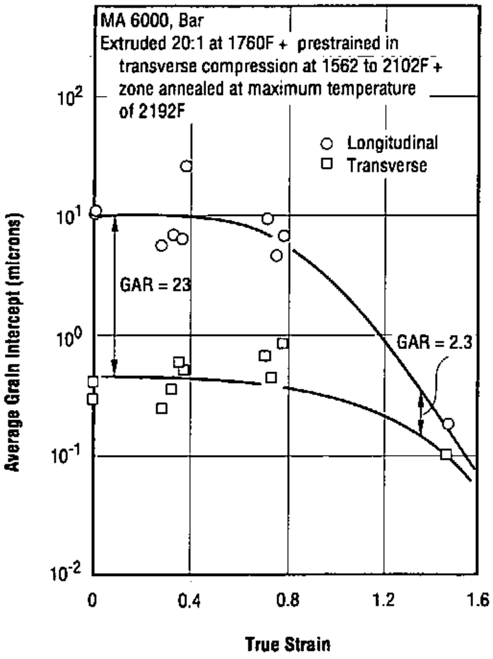

Fig. 1.5.2 Effects of prestraining on grain size and grain aspect ratio after zone annealing (Ref. 14)

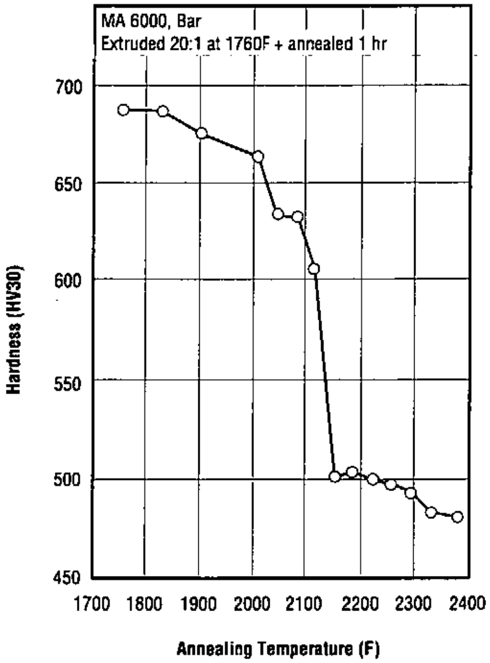

Fig. 1.6.1 Effect of annealing temperature on hardness (Ref. 14)

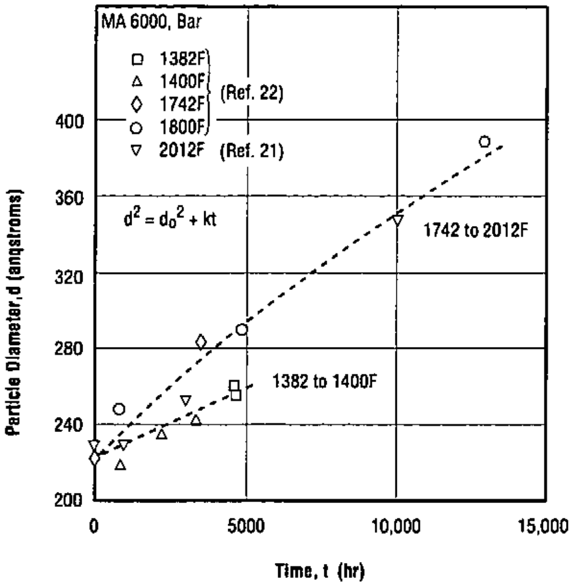

Fig. 2.1.2.1.1 Effects of exposure time on yttria dispersoid particle size at 1382 to 2012F (Refs. 21, 22)

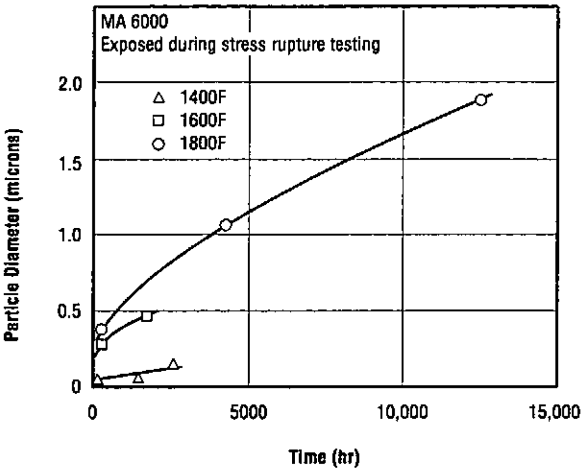

Fig. 2.1.2.1.2 Effects of exposure time on gamma-prime particle size at 1400 to 1800F (Ref. 22)

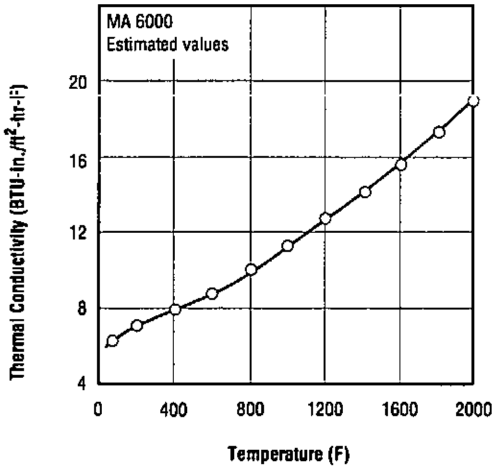

Fig. 2.1.3.1 Thermal conductivity (Ref. 1)

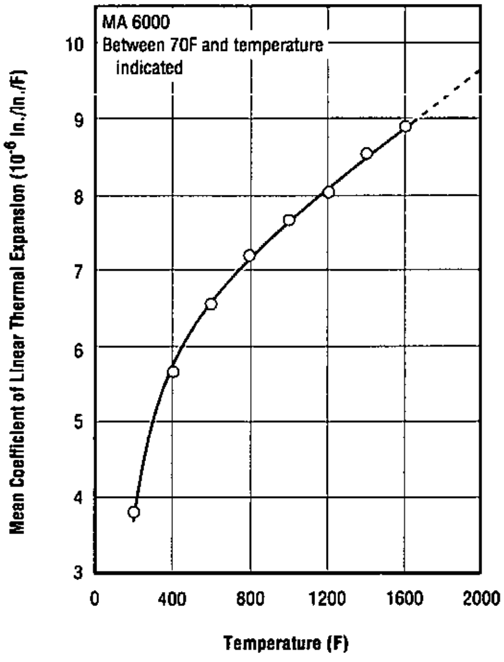

Fig. 2.1.4.1 Mean coefficient of linear thermal expansion (Ref. 1)

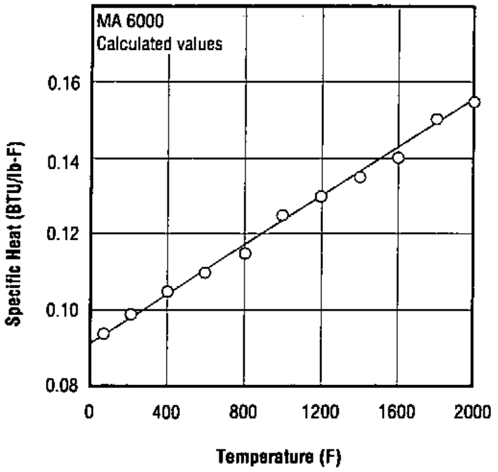

Fig. 2.1.5.1 Specific heat (Ref. 1)

Table 2.3.4.2 Cyclic oxidation resistance[a] at 2012F of MA 6000 compared with three other superalloys (Ref. 1)

Material	Condition	Weight Change (mg/cm^2)
MA 6000	Extruded + heat treated[b]	-14.1
IN 100	As cast	-7.3
IN 713LC	As cast	-22.1
IN 738	Heat treated[c]	-49.5

[a] Exposed for 504 hours at 2012F in air with 5 percent H_2O, thermal cycled by rapid cool to room temperature every 24 hours. Weight changes determined after descaling.

[b] 2250F, 0.5 hr, AC + 1750F, 2 hr, AC + 1550F, 24 hr, AC.

[c] 2050F, 0.5 hr + 1550F, 24 hr.

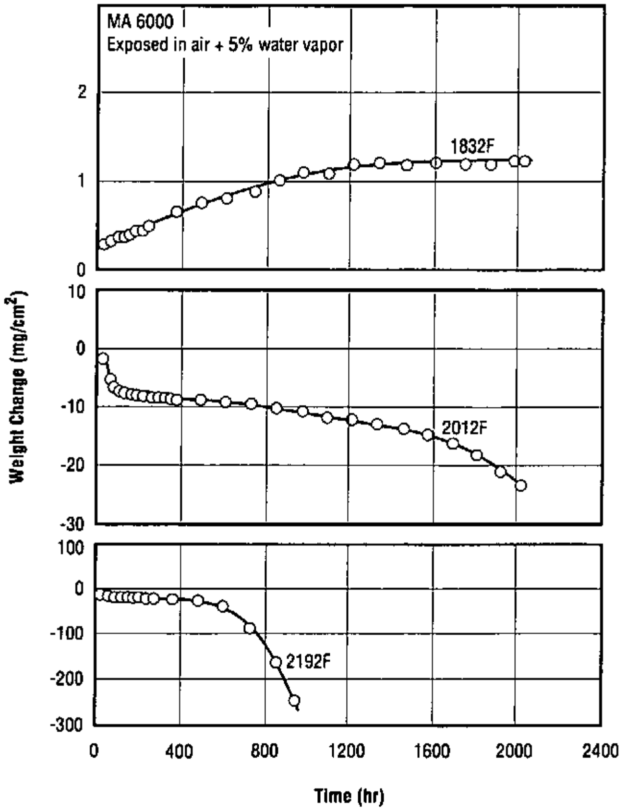

Fig. 2.3.4.1 Oxidation weight change behavior in air at elevated temperatures (Ref. 25)

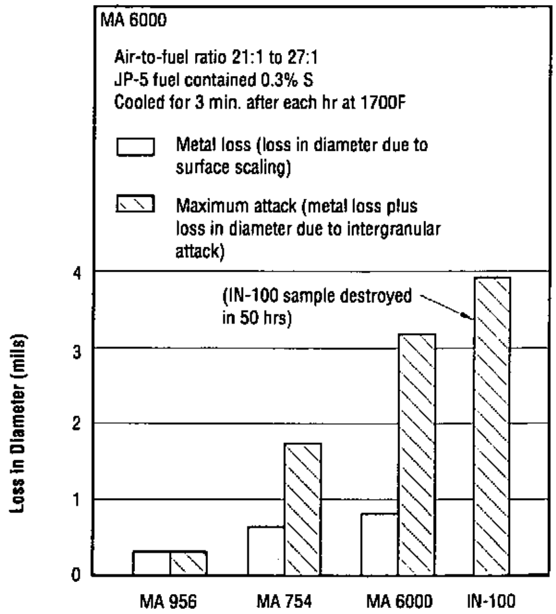

Fig. 2.3.4.3 Metal loss and maximum attack after burner rig testing for 500 hours at 1700F for MA 6000 and three other superalloys (Refs. 17, 26)

Table 2.3.4.4 Burner rig oxidation resistance[a] at 1700F of MA 6000 and three other superalloys (Ref. 1)

Material	Condition	Test Time (hr)	Weight Change (mg/cm^2)
MA 6000	Extruded + heat treated[b]	312	- 11.1
IN 100	As cast	48	- 367
IN 713LC	As cast	168	- 489
IN 738	Heat treated[c]	312	- 9.7

[a] Tested in JP-5 fuel with 0.3 percent sulfur and 5 ppm sea water with air-to-fuel ratio 30:1, thermal cycled by rapid cool to room temperature every 60 minutes. Weight changes determined after descaling.

[b] 2250F, 0.5 hr, AC + 1750F, 2 hr, AC + 1550F, 24 hr, AC.

[c] 2050F, 0.5 hr + 1550F, 24 hr.

Table 2.3.4.5 Burner rig oxidation resistance[a] at 1700 and 2000F (Ref. 25)

Material	Tested at 1700F, 312 hr		Tested at 2000F, 312 hr		Tested at 2000F, 500 hr	
	Metal Loss [b] (mil)	Maximum Attack [c] (mil)	Metal Loss (mil)	Maximum Attack (mil)	Metal Loss (mil)	Maximum Attack (mil)
Coated MA 6000[d]	1.6	2.0	4.2	4.7	7.6	8.4
Coated MA 6000[e]	—	—	0.4[f]	0.4[f]	6.9	6.9
MA 6000 (uncoated)	1.9[f]	2.2	3.6	14.1	—	—
MA 754 (uncoated)	0.6[f]	1.7	12.7	18.5	—	—
Mar-M 509 (uncoated)	0.7[f]	2.9	80.3	83.5	—	—

[a] Alloys tested in JP-5 fuel with 850 ppm sulfur and 5 ppm sea water, air-to-fuel ratio 30:1, thermal cycled by rapid cool to room temperature every 60 minutes.

[b] Metal loss is loss of diameter due to oxide and sulfide scale formation.

[c] Maximum attack is metal loss due to scaling plus depth of intergranular oxidation and sulfidation.

[d] Low pressure plasma sprayed coating of Ni-23Co-20Cr-8.5Al-0.6Y-4Ta, 7.5 mils thick.

[e] Underlayer of Ni-20Cr-5Al-5.5Ta between substrate and outer coating as in footnote "d".

[f] Diameter increased during exposure due to adherent scale.

Table 2.3.4.6 Frictional ignition of MA 6000 and other aerospace alloys[a] (Ref. 27)

Material	**Average Mechanical Energy Required for Ignition[b] (W/in.^{2} x 10^{-12})**
MA 754	>26.5[c]
Inconel 600	16.1
MA 6000	14.7
Waspaloy	13.1
Monel K-500	9.7
Hastelloy X	7.7
Inconel 718	7.2
Incoloy 909	6.9
Type 304 Stainless Steel	6.7
Inconel 706	6.5
MA 956	4.4
Type 440C Stainless Steel	4.0

[a] Pairs of hollow cylinders pressed together with one cylinder fixed and the other rotating at 17,000 rpm in 1000 psig oxygen.

[b] Mechanical energy equals Pv product, where P = contact pressure (psi) and v = linear surface velocity (ips).

[c] No ignition.

Table 3.2.7.1.1 Effects of notches on room temperature tensile properties in helium and in hydrogen (Ref. 1)

Alloy			MA 6000				
Form			Thermo-mechanically Processed Bar				
Processing			Annealed 2250F, 0.5 hr, AC + 1750F, 2 hr, AC + 1550F, 24 hr, AC				
Specimen Surface	**Atmosphere[a]**	**Orientation**	**F_{ty} (ksi)**	**F_{tu} (ksi)**	**Elongation (percent)**	**RA (percent)**	**H_2/He Strength Ratio**
Smooth	He	L	169.2	169.3	0.75	2.0	—
		T	171.8	171.9	0	3.9	—
	H_2	L	165.8	165.9	0.6	3.9	0.98
		T	175.0	175.0	1.4	2.0	0.98
Notched[b]	He	L	—	157.4	—	0.8	—
		T	—	122.4	—	0	—
	H_2	L	—	134.6	—	1.2	0.86
		T	—	122.4	—	—	0.92

[a] Gas pressure 5000 psi.

[b] Notch dimensions not reported.

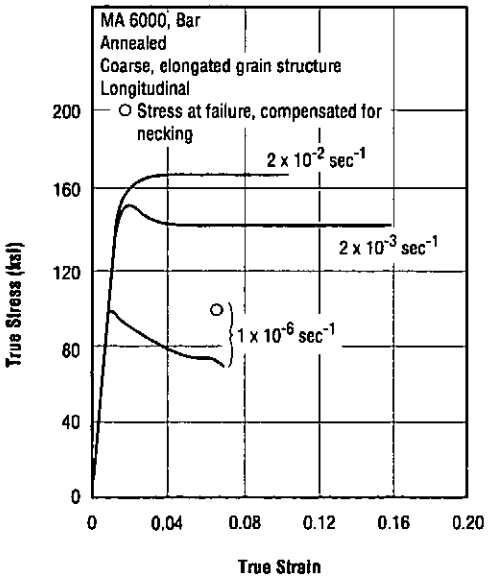

Fig. 3.3.1.1 Effect of strain rate on tensile stress-strain diagrams for coarse-grained alloy at 1400F (Ref. 28)

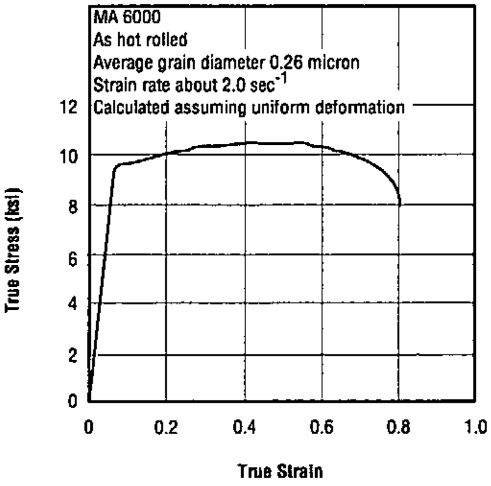

Fig. 3.3.1.2 Tensile stress-strain diagram for fine-grained alloy at 2012F (Ref. 30)

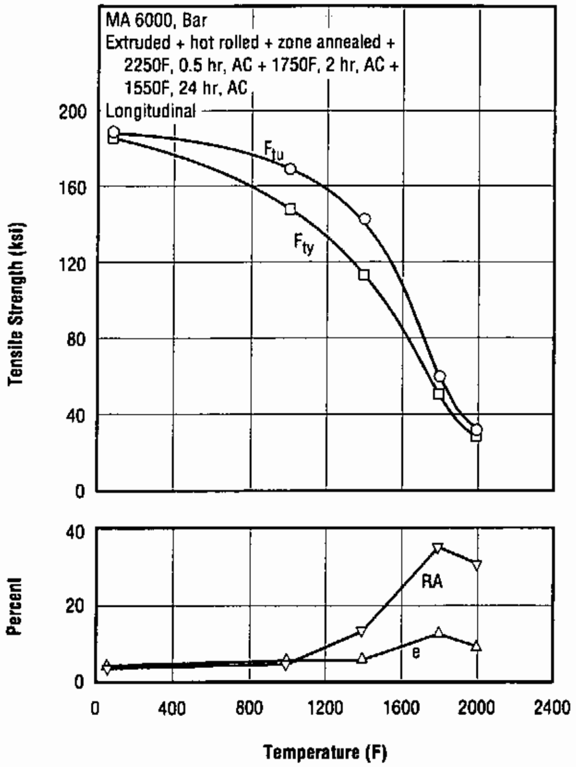

Fig. 3.3.1.3 Effects of temperature on longitudinal tensile properties of annealed bar (Ref. 1)

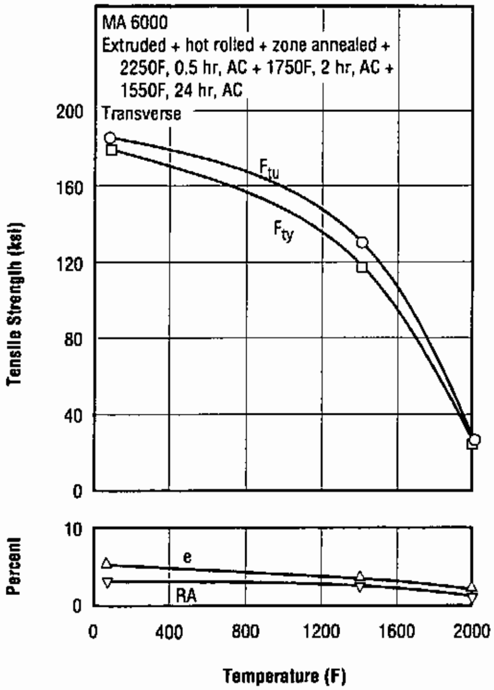

Fig. 3.3.1.4 Effects of temperature on transverse tensile properties of annealed bar (Ref. 1)

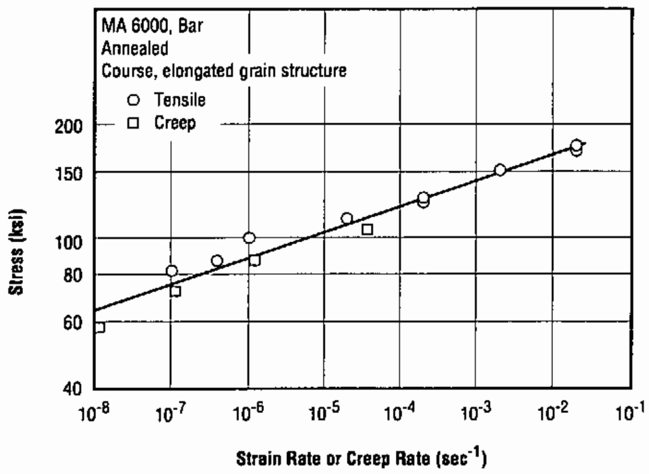

Fig. 3.3.1.5 Variation of strength with strain rate or creep rate at 1400F (Ref. 28)

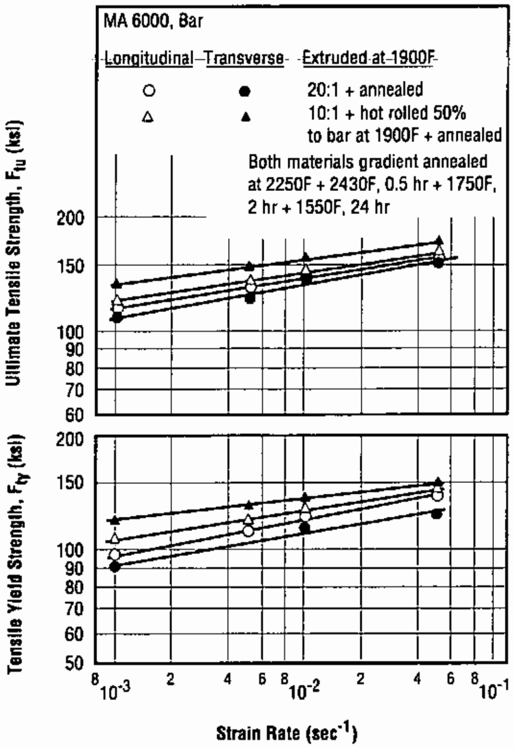

Fig. 3.3.1.6 Effects of strain rate, orientation, and fabrication method on tensile strength at 1400F (Ref. 29)

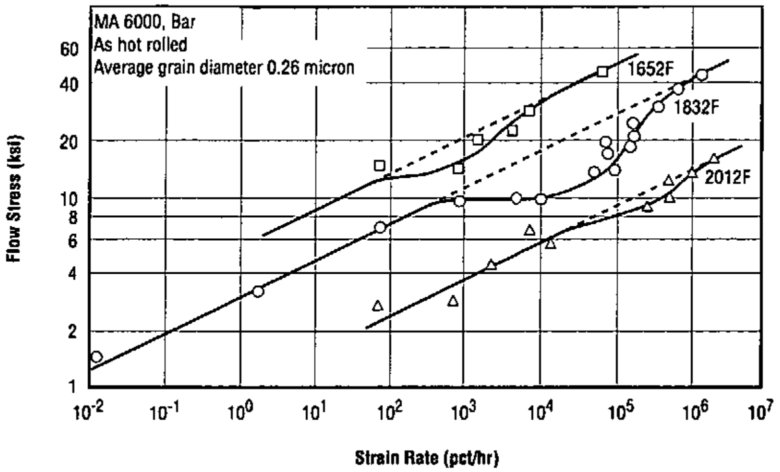

Fig. 3.3.1.7 Effects of strain rate and temperature on flow stress of fine-grained alloy (Ref. 30)

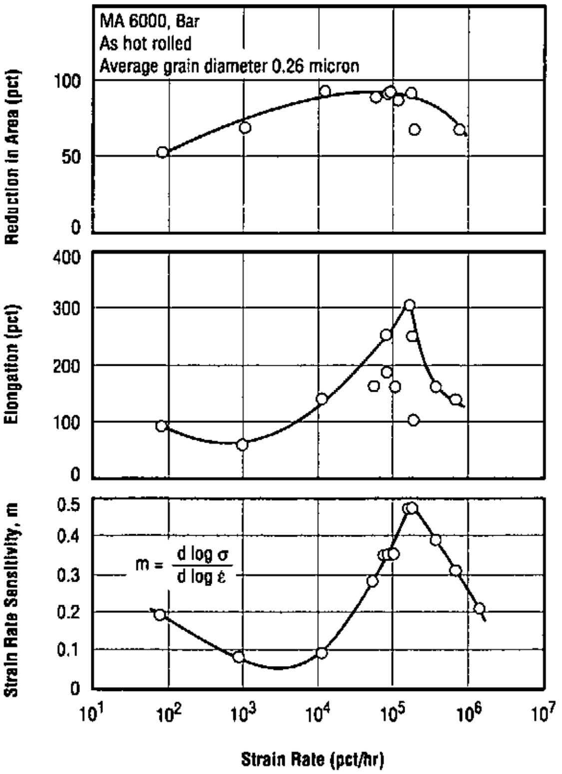

Fig. 3.3.1.8 Effects of strain rate on tensile strain rate sensitivity and ductility of fine-grained alloy at 1832F (Ref. 30)

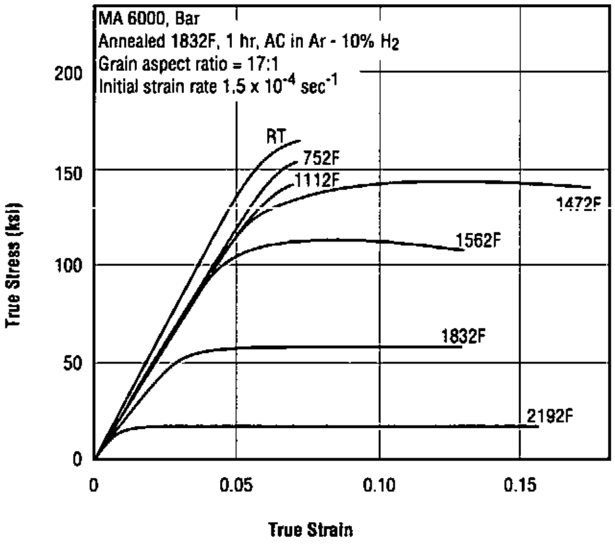

Fig. 3.3.2.1 Compressive stress-strain diagrams at room temperature to 2192F (Ref. 31)

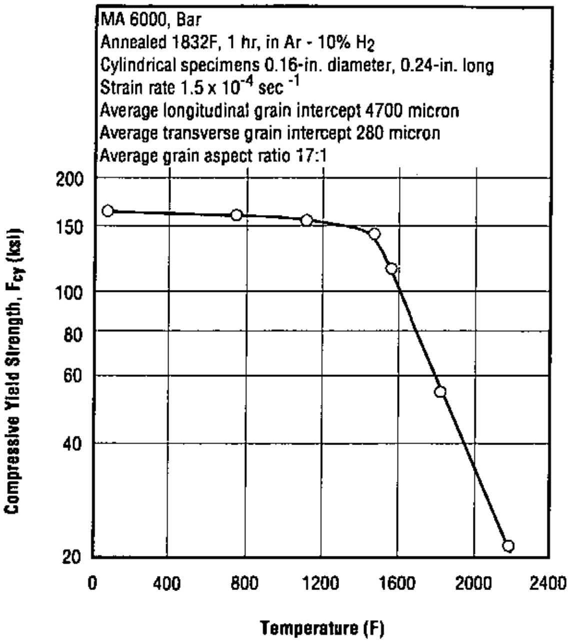

Fig. 3.3.2.2 Effects of temperature on compressive 0.2-percent yield strength (Ref. 31)

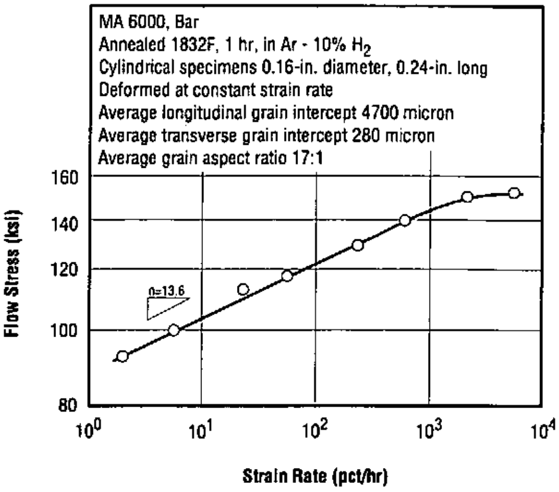

Fig. 3.3.2.3 Effects of strain rate on compressive steady state flow stress at 1562F (Ref. 31)

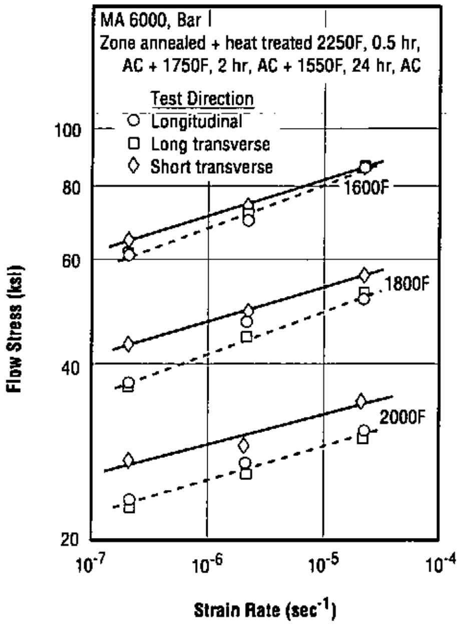

Fig. 3.3.2.4 Effects of orientation and temperature on compressive steady state flow stress (Ref. 32)

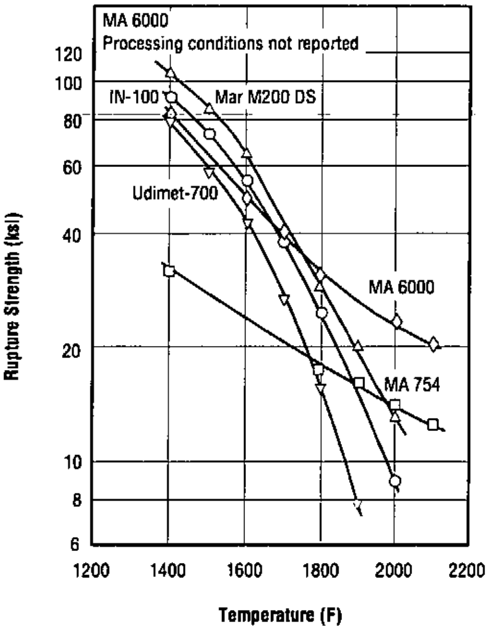

Fig. 3.4.1 Effects of temperature on 100-hour rupture strength of MA 6000, MA 754, and three non-ODS superalloys (Ref. 62)

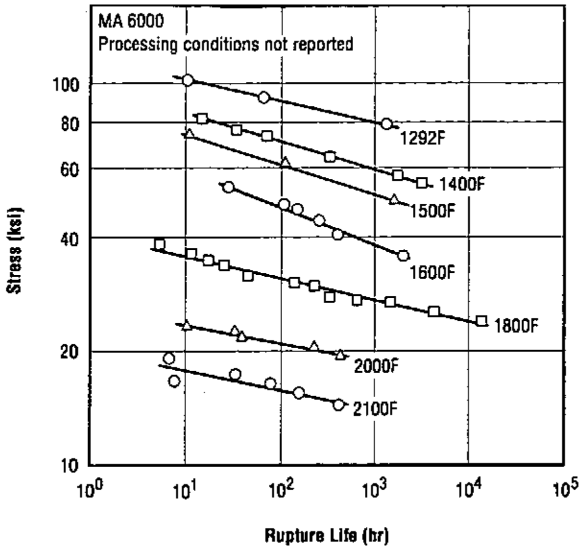

Fig. 3.4.2 Creep rupture behavior at 1292 to 2100F (Ref. 63)

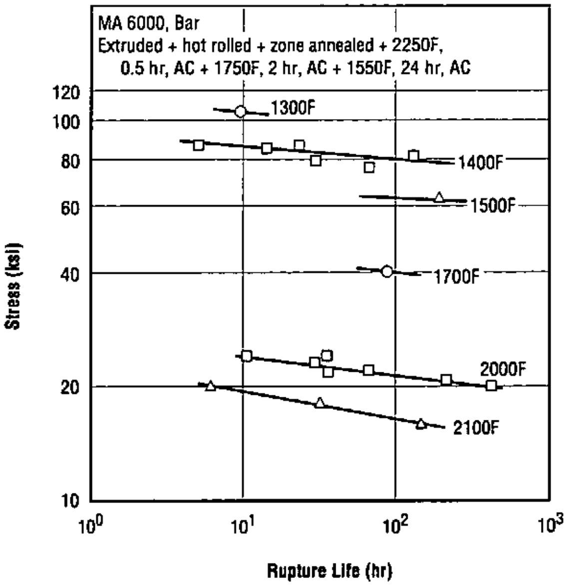

Fig. 3.4.3 Longitudinal creep rupture behavior of annealed bar at 1300 to 2100F (Ref. 1)

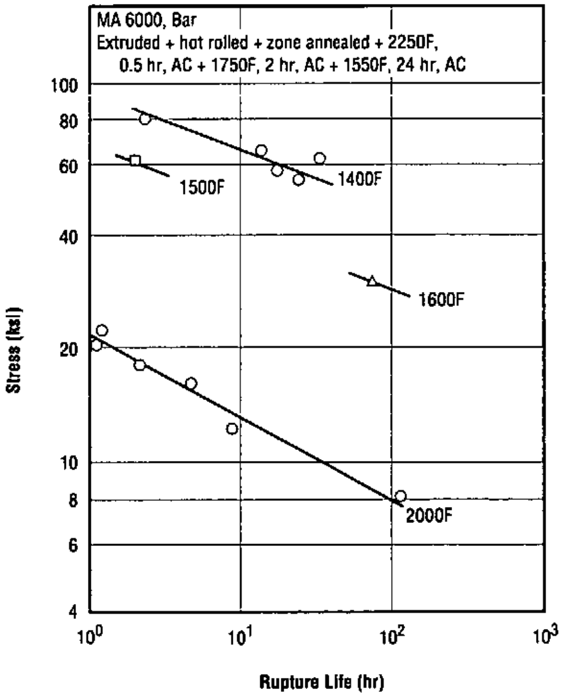

Fig. 3.4.4 Transverse creep rupture behavior of annealed bar at 1400 to 2000F (Ref. 1)

Table 3.4.5 Creep rupture properties of annealed bar at 1400 and 2000F (Ref. 1)

Alloy			MA 6000						
Form			Bar, Extruded + Hot-rolled						
Heat Treatment			Zone Annealed + 2250F, 0.5 hr, AC + 1750F, 2 hr, AC + 1550F, 24 hr, AC						
Temperature (F)	**Stress (ksi)**	**Steady Creep Rate (pct/hr)**	**Time (hr) for Total Creep Strain of:**				**Rupture Life (hr)**	**Elongation (percent)**	**Reduction in Area (percent)**
			0.1 percent	**0.2 percent**	**0.5 percent**	**1.0 percent**			
1400	74	4.14×10^{-3}	15.0	40.0	108.0	184.0	293.3	4.0	6.3
	78	1.34×10^{-2}	1.5	4.0	25.0	60.0	154.8	4.1	5.2
	80	1.15×10^{-2}	2.0	7.0	32.5	75.5	132.4	3.3	3.2
	82	2.07×10^{-2}	1.5	5.0	16.5	43.0	98.1	3.5	3.6
2000	22	2.00×10^{-3}	10.0	25.0	320.0	575.0	589.7	1.3	9.4
	23	6.95×10^{-3}	3.5	7.8	27.0	78.5	96.5	2.6	7.0

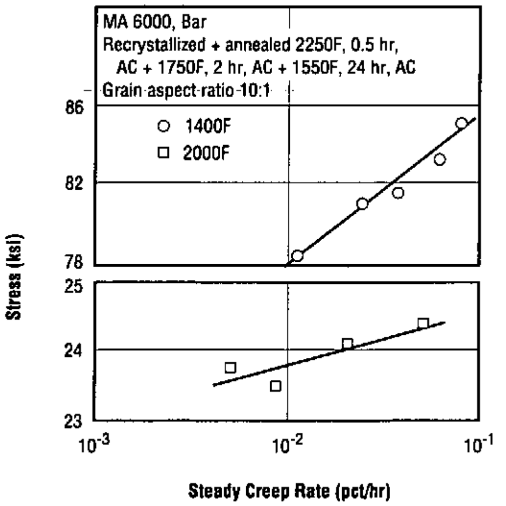

Fig. 3.4.6 Creep rate behavior of annealed bar at 1400 and 2000F (Refs. 34, 62)

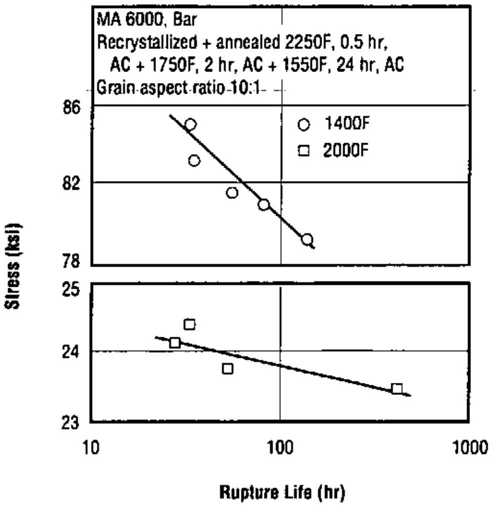

Fig. 3.4.7 Rupture life behavior of annealed bar at 1400 and 2000F (Refs. 34, 62)

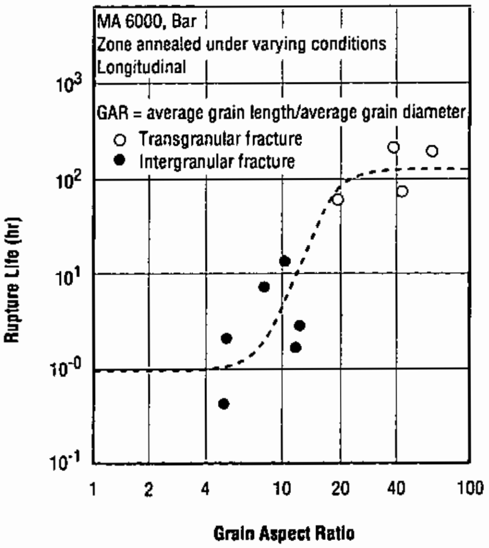

Fig. 3.4.8 Effects of grain aspect ratio on rupture life at 1742F and 33.4 ksi (Refs. 35, 37)

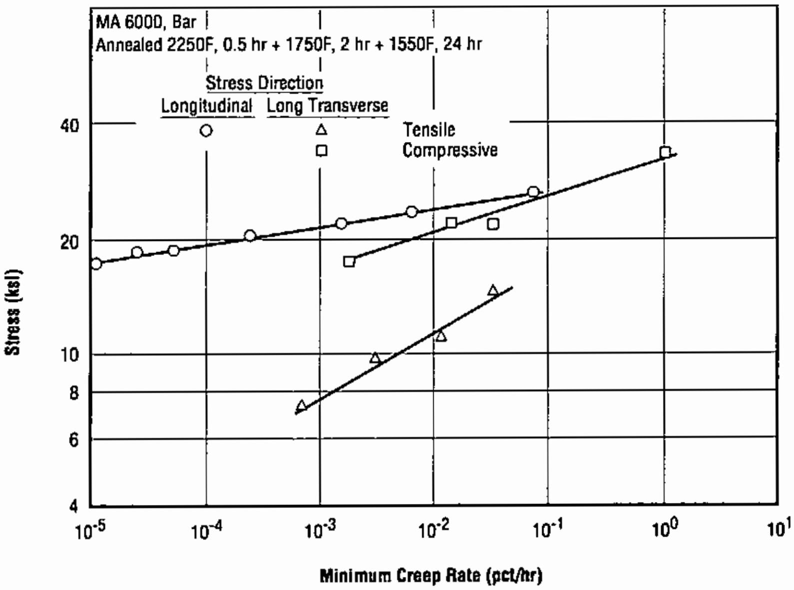

Fig. 3.4.9 Effects of orientation on tensile and compressive creep rate behavior at 1922F (Refs. 37, 38)

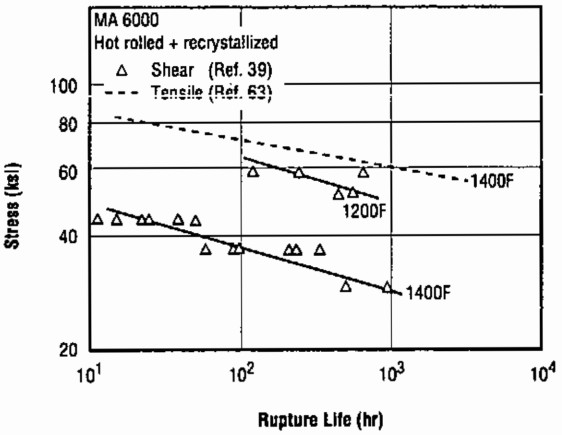

Fig. 3.4.10 Shear and tensile creep rupture behavior (Refs. 39, 63)

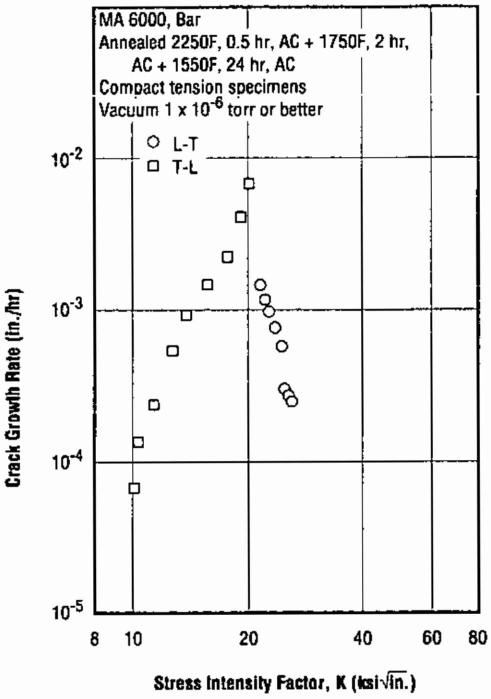

Fig. 3.4.11 Effect of orientation on creep crack growth rates in vacuum at 1832F (Ref. 40)

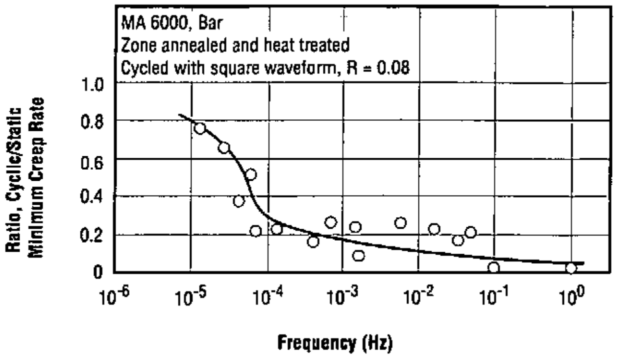

Fig. 3.4.12 Effects of load cycling on creep rate of annealed bar at 1400F and maximum stress of 77 ksi (Ref. 41)

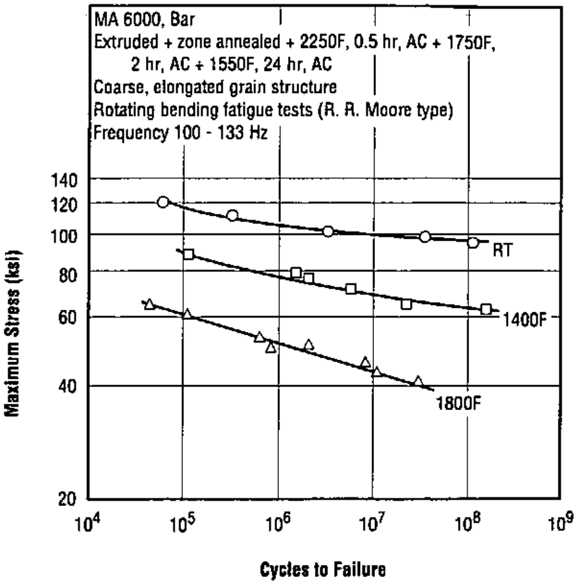

Fig. 3.5.1.1 High-cycle fatigue behavior at room and elevated temperatures (Ref. 42)

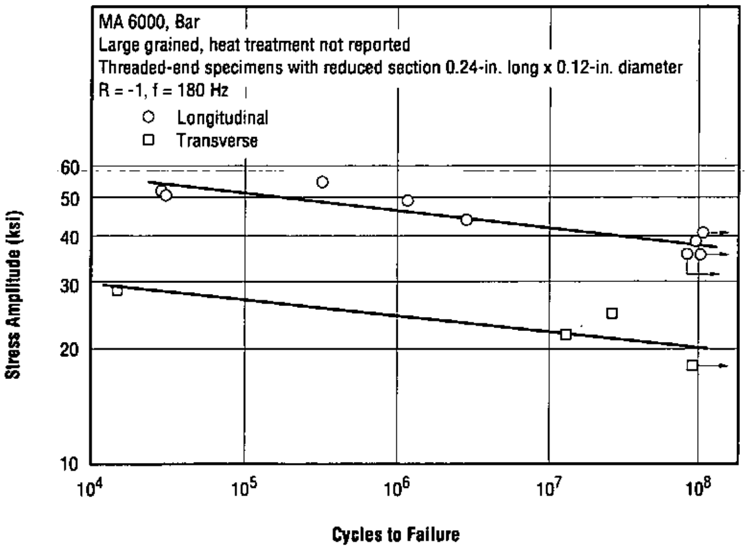

Fig. 3.5.1.2 Effect of orientation on high-cycle fatigue behavior at 1562F (Ref. 43)

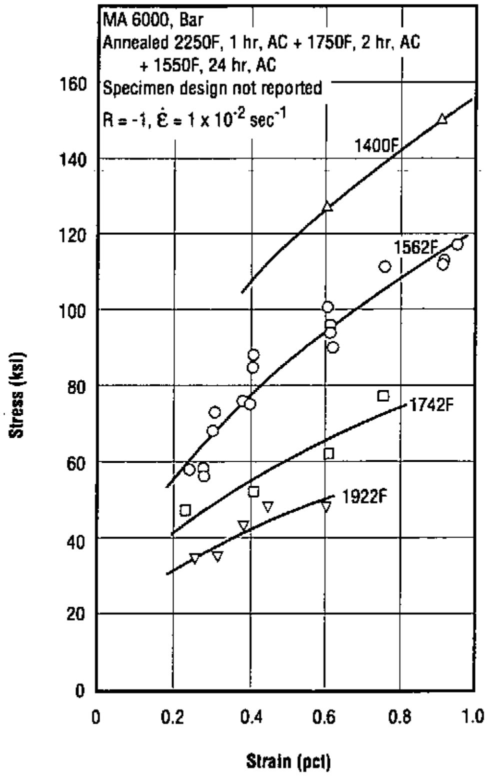

Fig. 3.5.2.1 Effect of temperature on cyclic stress-strain curves at 1400 to 1922F (Ref. 44)

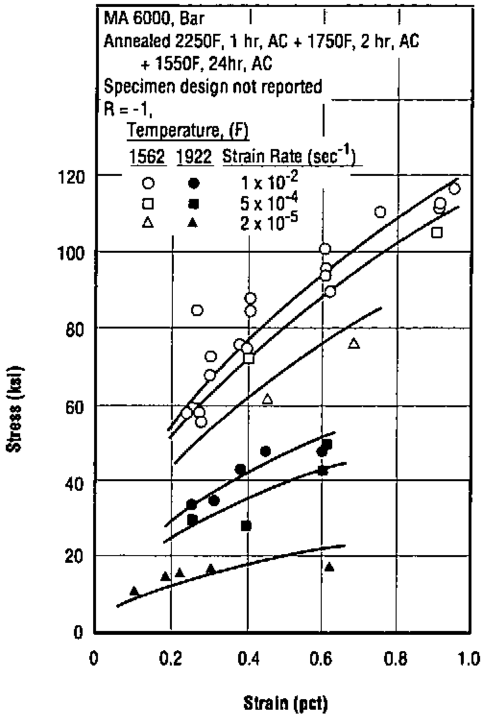

Fig. 3.5.2.2 Effects of strain rate on cyclic stress-strain curves at 1562 to 1922F (Ref. 44)

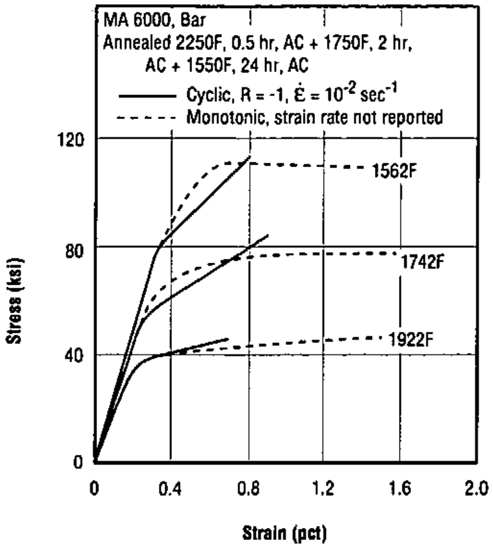

Fig. 3.5.2.3 Cyclic and monotonic stress-strain curves at 1562 to 1922F (Ref. 45)

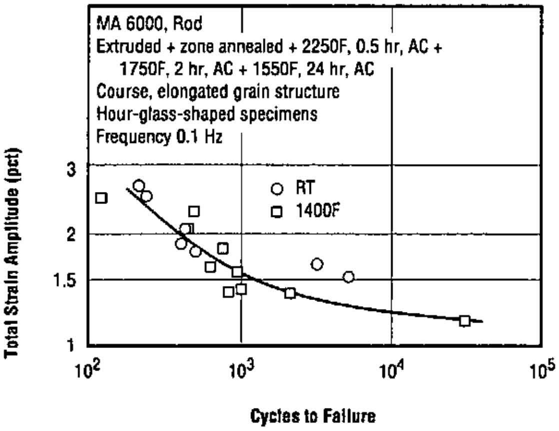

Fig. 3.5.2.4 Low-cycle fatigue behavior at room temperature and 1400F (Ref. 42)

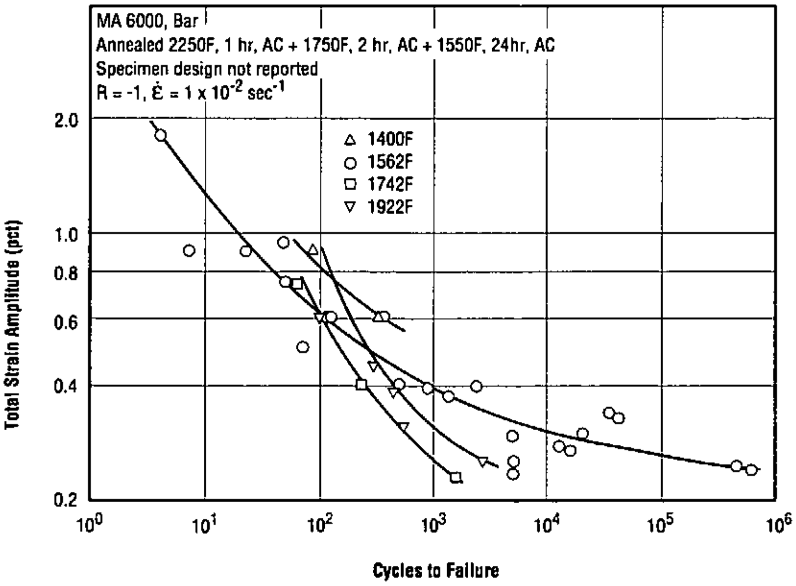

Fig. 3.5.2.5 Effect of temperature on low-cycle fatigue behavior at 1400 to 1922F (Ref. 44)

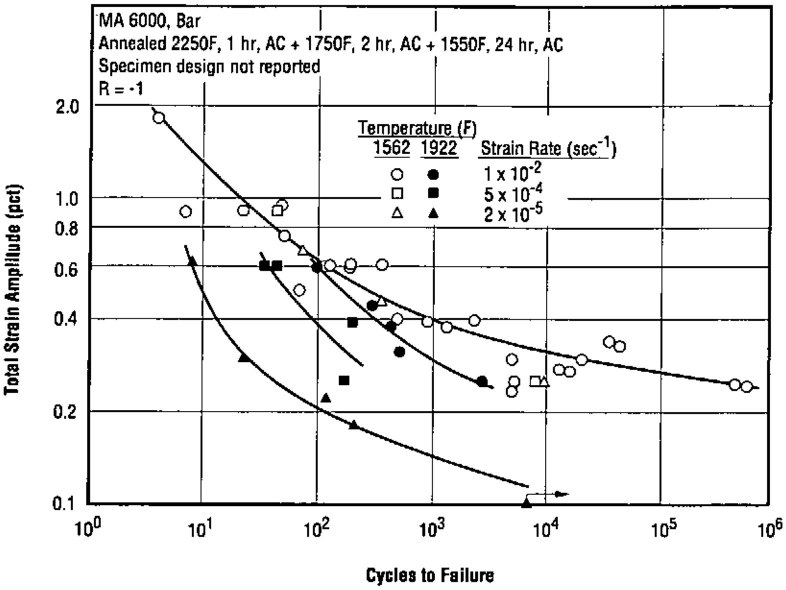

Fig. 3.5.2.6 Effects of strain rate on low-cycle fatigue behavior at 1562 and 1922F (Ref. 44)

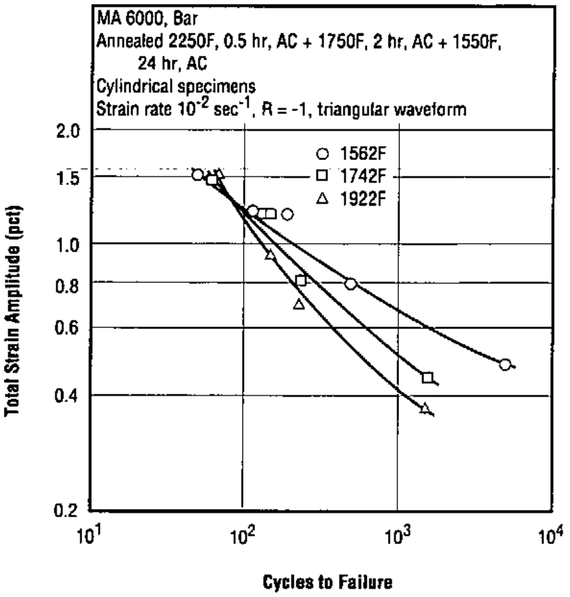

Fig. 3.5.2.7 Low-cycle fatigue behavior at elevated temperatures in air (Ref. 47)

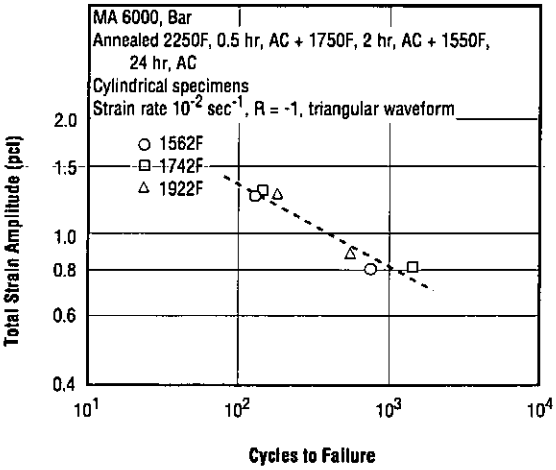

Fig. 3.5.2.8 Low-cycle fatigue behavior at elevated temperatures in vacuum (Ref. 47)

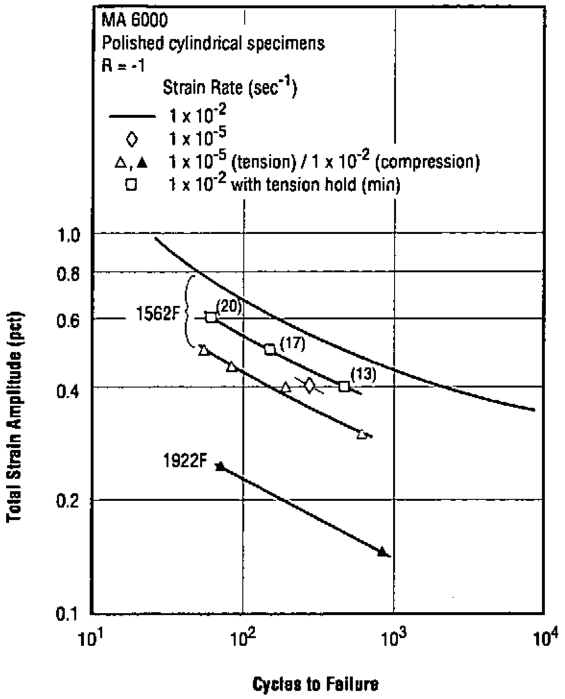

Fig. 3.5.2.9 Effects of strain rate and loading asymmetry on low-cycle fatigue behavior at 1562 and 1922F (Refs. 3, 49)

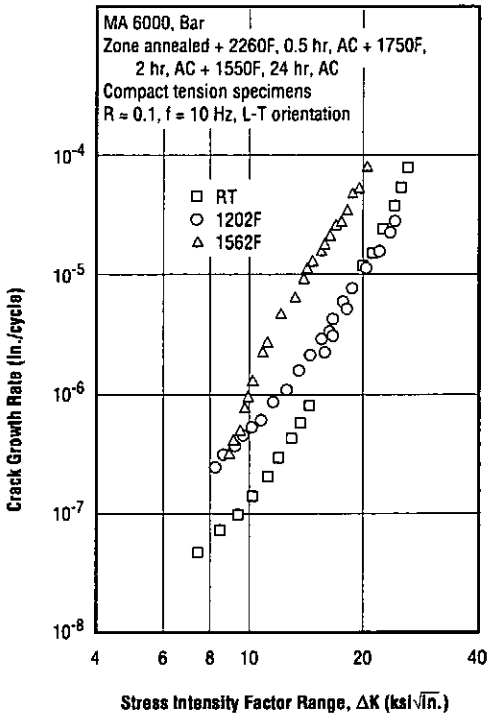

Fig. 3.5.3.1 Effect of temperature on fatigue crack growth rates at room temperature to 1562F (Ref. 50)

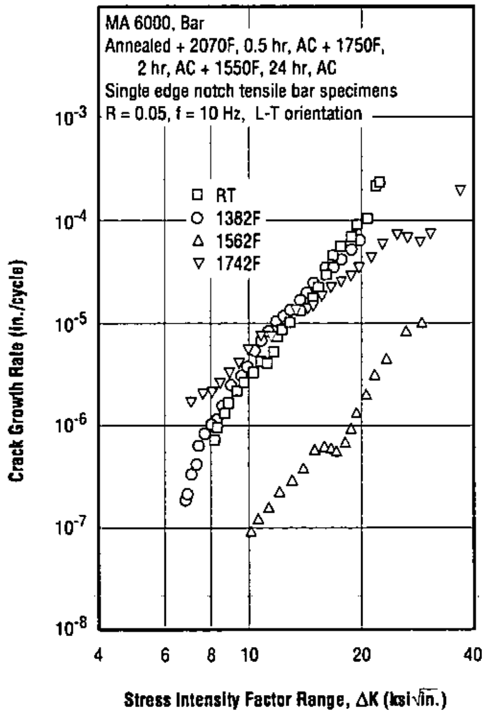

Fig. 3.5.3.2 Effect of temperature on fatigue crack growth rates at room temperature to 1742F (Ref. 51)

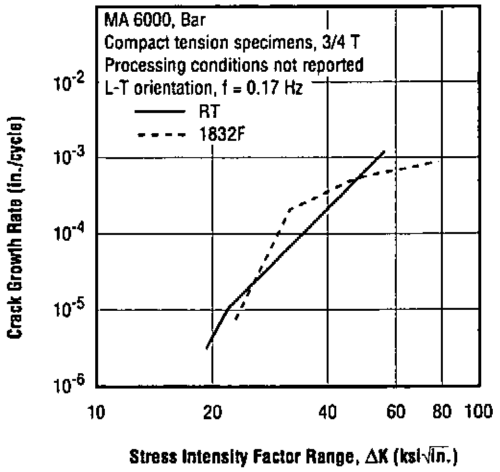

Fig. 3.5.3.3 Effect of temperature on fatigue crack growth rates at room temperature and 1832F (Ref. 52)

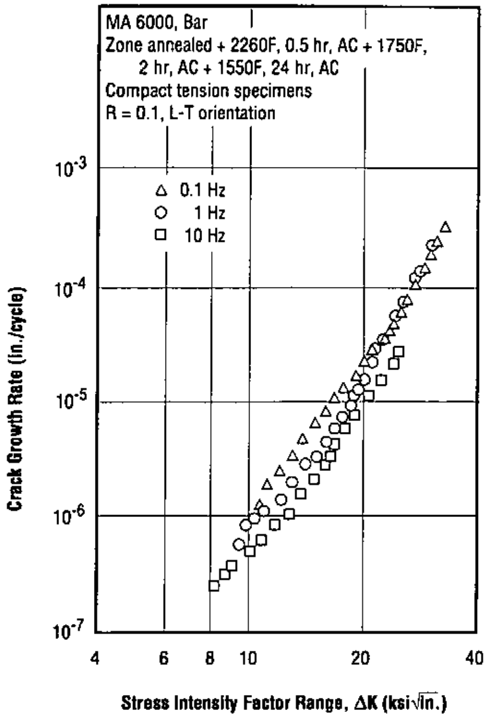

Fig. 3.5.3.4 Effect of frequency on fatigue crack growth rates at 1202F (Ref. 50)

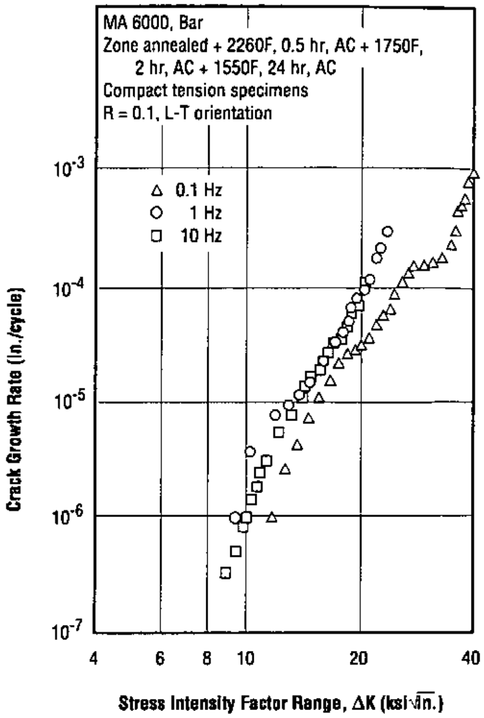

Fig. 3.5.3.5 Effect of frequency on fatigue crack growth rates at 1562F using compact tension specimens (Ref. 50)

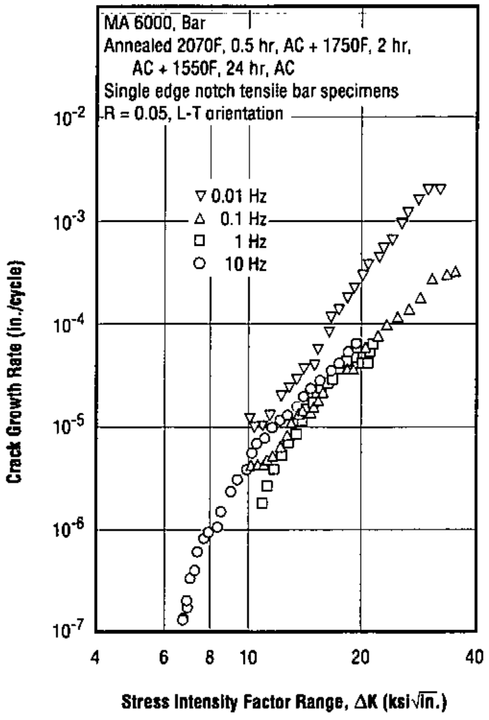

Fig. 3.5.3.6 Effect of frequency on fatigue crack growth rates at 1562F using edge notch tensile specimens (Ref. 51)

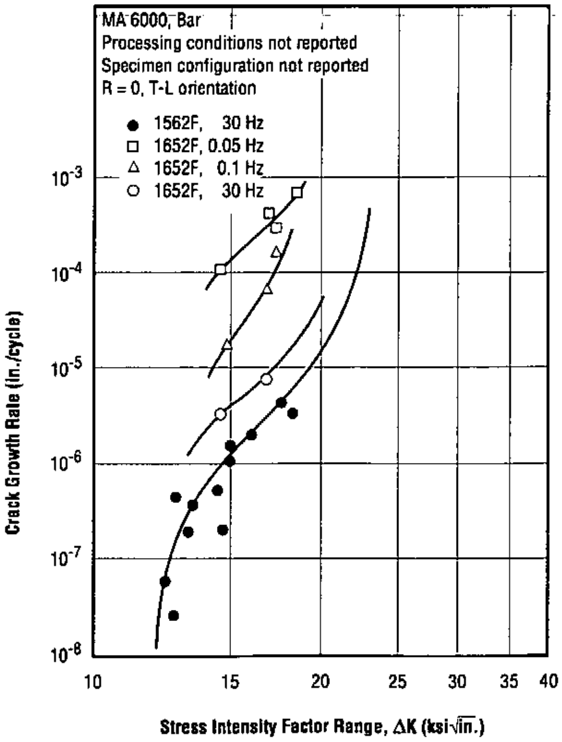

Fig. 3.5.3.7 Effects of temperature and frequency on fatigue crack growth rates (Ref. 2)

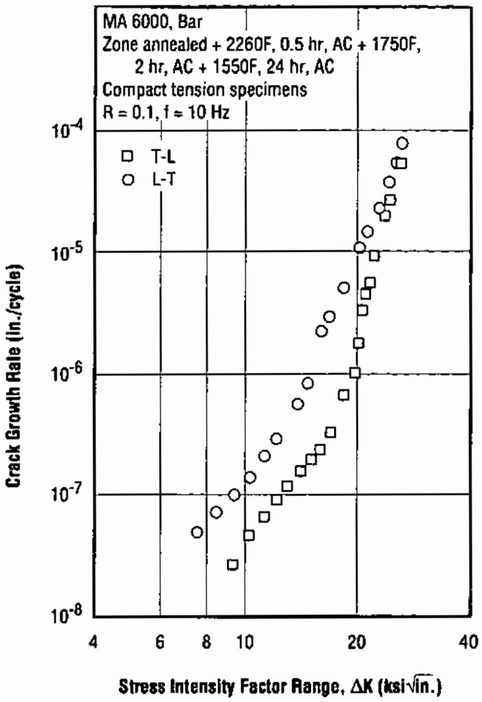

Fig. 3.5.3.8 Effect of specimen orientation on fatigue crack growth rates at room temperature (Ref. 50)

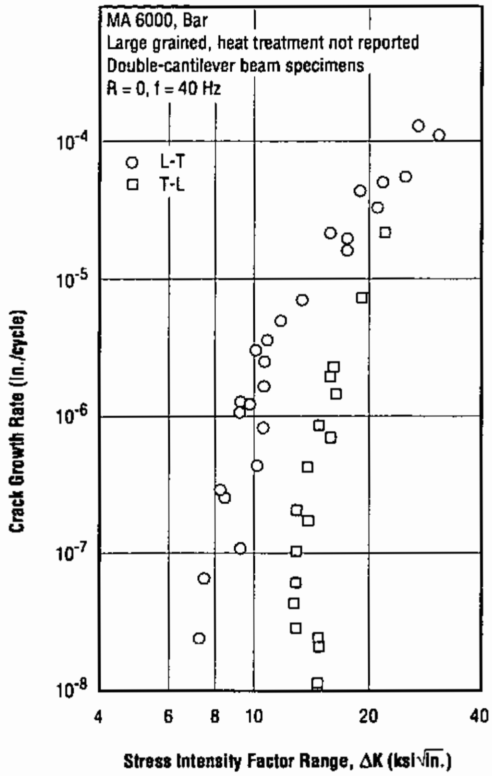

Fig. 3.5.3.9 Effect of specimen orientation on fatigue crack growth rates at 1562F (Ref. 43)

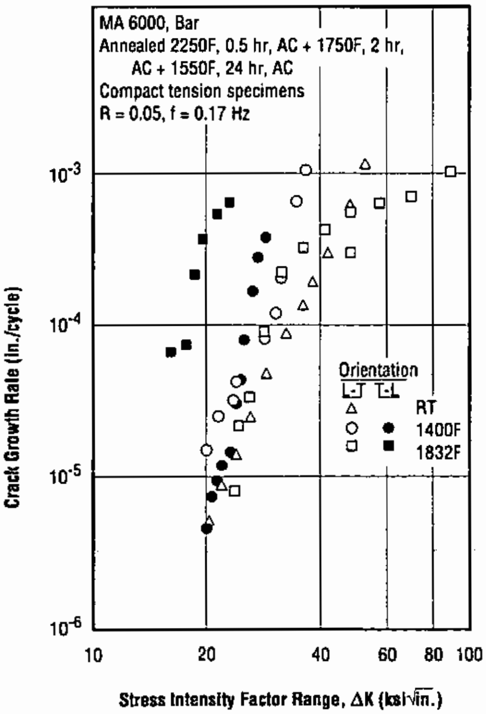

Fig. 3.5.3.10 Effects of temperature and orientation on fatigue crack growth rates (Ref. 40)

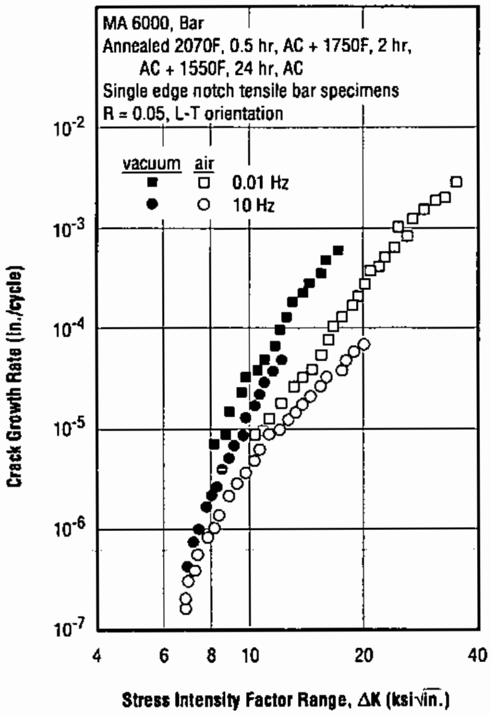

Fig. 3.5.3.11 Effects of environment and two different frequencies on fatigue crack growth rates at 1562F (Ref. 53)

Table 3.5.4.1 Thermal fatigue behavior of MA 6000 compared with several other superalloys (Refs. 1, 42)

Material	**Cycles to First Crack**
MA 6000[a]	10,250
MA 6000, coated [b]	12,750
DS IN 100[c]	2,400
B 1900	400
Mar-M 509	238
IN 738	100

Note: Fluidized bed cycling in air between 600 and 1990F with 3-minute hold at each temperature. Double wedge specimens with wedge radii of 0.039 and 0.28 in.

[a] Bar, extruded + hot rolled + zone annealed + 2250F, 0.5 hr, AC + 1750F, 2 hr, AC + 1550F, 24 hr, AC.

[b] NiCrAlY coating.

[c] Directionally solidified.

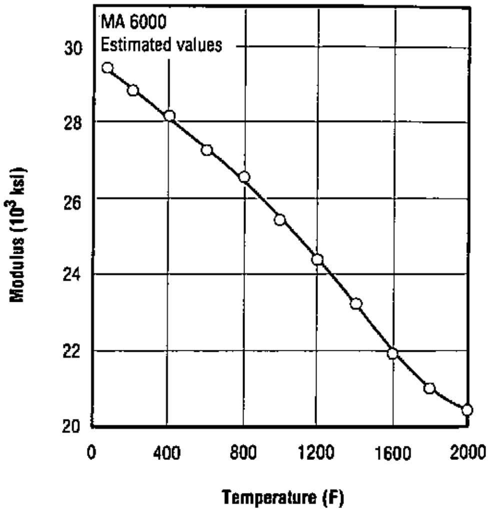

Fig. 3.6.2.1 Modulus of elasticity (Ref. 1)

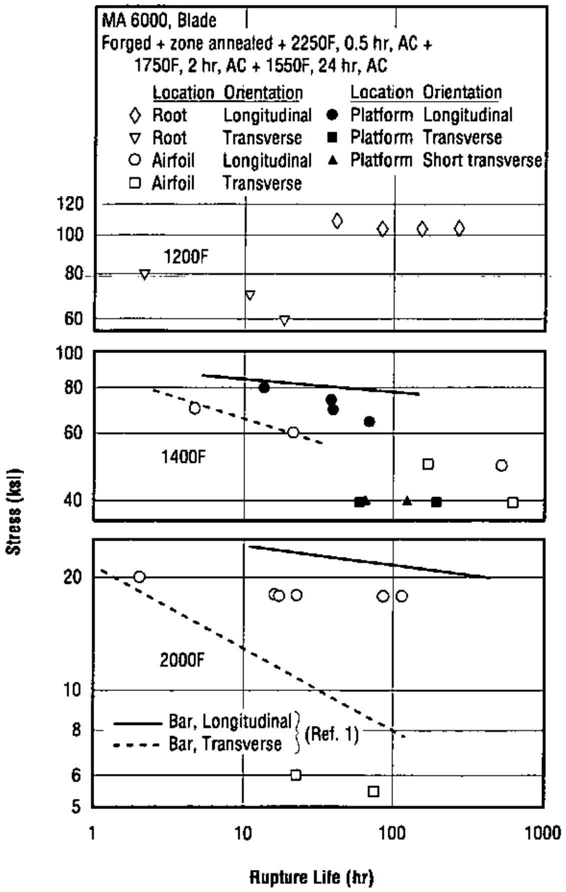

Fig. 4.1.1 Effects of temperature and orientation on rupture life at several locations on forged and annealed blade and comparison with annealed bar (Refs. 1, 58)

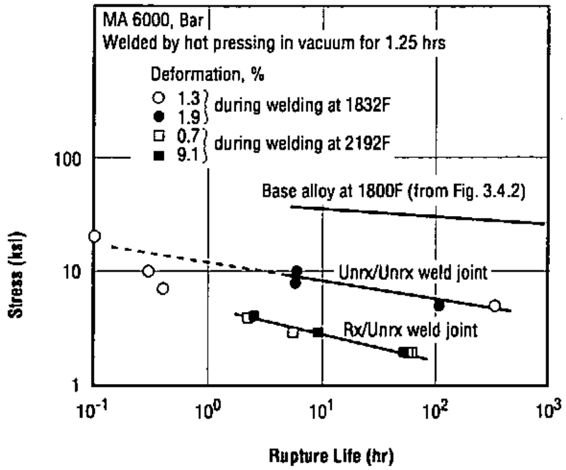

Fig. 4.3.1 Effects of recrystallization and welding parameters on rupture strength of hot press diffusion welded joints at 1832F (Ref. 60)

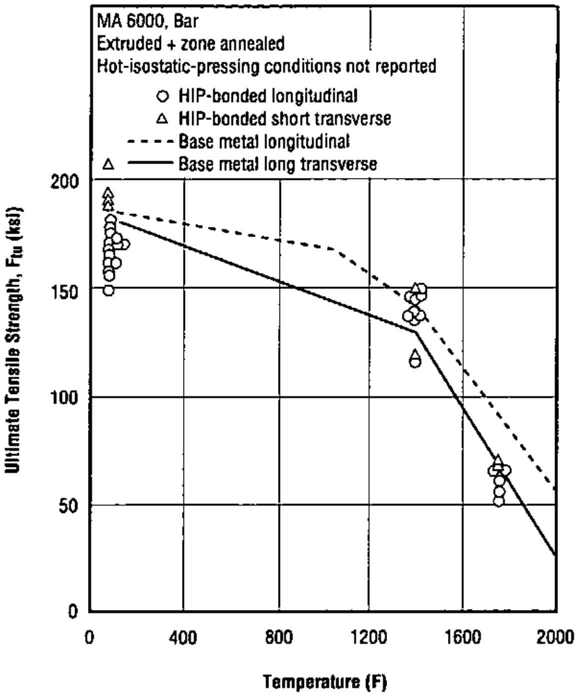

Fig. 4.3.2 Tensile strength of hot-isostatic-press diffusion welded joints at room and elevated temperatures (Ref. 61)

References

1. "INCONEL alloy MA 6000," Trade Literature, INCO Alloys International, Huntington, WV 25720, pp. 10 (undated).
2. Nazmy, M.; Heffelner, W.; and Wuthrich, C., "Elevated Temperature Creep-Fatigue Crack Propagation in Nickel-Base Alloys and 1Cr-Mo-V Steel," *Metallurgical Transactions*, Vol. 19A, pp. 855-862 (April 1991).
3. Elzey, D.M., and Arzt, E., "Crack Initiation and Propagation During High-Temperature Fatigue of Oxide Dispersion-Strengthened Superalloys," *Metallurgical Transactions*, Vol. 22A, pp. 837-851 (April 1991).
4. Benn, R.C.; Curwick L.R.; and Hack, G.A.J., "Scale-Up Thermomechanical Processing of MA 6000E," *Powder Metallurgy*, No. 1, 24, No. 4, pp. 191-195 (1981).
5. Grundy, E., and Bomford, M.J., "Forged Turbine Components in O.D.S. Nickel Base Superalloys," presented at Conference on Advanced Materials and Processing Techniques for Structural Applications, Paris, France, pp. 357-366 (September 7-9, 1987).
6. "MA Alloy Picked for Turbine Blades," *Advanced Materials & Processes*, Vol. 143, No. 3, p. 9 (March 1993).
7. "Inconel Alloy MA 6000 (Mechanically Alloyed Nickel-Base Alloy)," *Alloy Digest*, Filing Code: Ni-288, pp. 2 (July 1983).
8. Vaccari, J.A., "Tackling a New Breed of Superalloys," *American Machinist*, Vol. 128, No. 12, pp. 64-65 (December 1984).
9. Hotzler, R.K., and Glasgow, T.K., "The Influence of Gamma Prime on the Recrystallization of an Oxide Dispersion Strengthened Superalloy - MA 6000E," *Metallurgical Transactions*, Vol. 13A, No. 10, pp. 1665-1674 (October 1982).
10. Singer, R.F., and Arzt, E., "Structure, Processing, and Properties of ODS Superalloys," presented at Conference on High Temperature Alloys for Gas Turbines and Other Applications, 1986, Part I, Liege, Belgium, pp. 97-126 (October 6-9, 1986).
11. Baloch, M.M., and Bhadeshia, H.K.D.H., "Directional Recrystallization in Inconel MA 6000 Nickel Base Oxide Dispersion Strengthened Superalloy," *Materials Science and Technology*, Vol. 6, No. 12, pp. 1236-1246 (December 1990).
12. Hotzler, R.K., and Glasgow, T.K., "Recrystallization Characteristics of Oxide Dispersion Strengthened Nickel-Base Alloys," presented at AIME/ASM Fourth International Symposium on Superalloys, Superalloys 1980, Champion, PA, pp. 455-464 (September 21-25, 1980).
13. Benjamin, J.S., "Mechanical Alloying - a Perspective," *Metal Powder Reports*, Vol. 45, No. 2, pp. 122-127 (February 1990).
14. Singer, R.F., and Gessinger, G.H., "The Influence of Hot Working on the Subsequent Recrystallization of a Dispersion Strengthened Superalloy - MA 6000," *Metallurgical Transactions*, Vol. 13A, No. 8, pp. 1463-1470 (August 1982).
15. Marsh, J.M., and Martin, J.W., "Micromechanisms of Texture Development During Zone Annealing of MA 6000 Extrusions," *Materials Science and Technology*, Vol. 7, No. 2, pp. 183-188 (February 1991).
16. White, C., "Oxide Dispersion Strengthened (ODS) Alloys," Research and Development of High Temperature Materials for Industry, pp. 71-78 (1989).
17. de Barbadillo, J.J., and Fischer, J.J., "Dispersion-Strengthened Nickel-Base and Iron-Base Alloys," Metals Handbook, Tenth Edition, Vol. 2, pp. 943-949 (1990).
18. Fleetwood, M.J., "Mechanical Alloying - The Development of Strong Alloys," *Materials Science and Technology*, Vol. 2, No. 12, pp. 1176-1182 (December 1986).
19. Sundaresan, R., and Froes, F.H., "Mechanical Alloying," *Journal of Metals*, Vol. 39, No. 8, pp. 22-27 (August 1987).
20. Hack, G.A.J., "Inconel Alloy MA 6000 - A New Material for High Temperature Turbine Blades," *Metal Powder Reports*, Vol. 36, No. 9, pp. 425-429 (September 1981).
21. Schaffer, G.B.; Loretto, M.H.; Smallman, R.E.; and Brooks, J.W., "The Stability of the Oxide Dispersion in Inconel Alloy MA 6000," *Acta Metallurgica*, Vol. 37, No. 9, pp. 2551-2558 (September 1989).
22. Benn, R.C., and Kang, S.K., "Long-Term Mechanical Behavior of Some ODS Alloys," presented at Fifth International Symposium on Superalloys, Superalloys 1984, Champion, PA, pp. 319-326 (October 7-11, 1984).
23. Smith, G.D., and Benn, R.C., "High Temperature Corrosion of LPPS-Coated Inconel MA 6000," *Surface Coating Technology*, Vol. 32, No. 1-4, pp. 201-214 (November 1987).
24. Lowell, C.E., and Barrett, C.A., "The Oxidation and Corrosion of ODS Alloys," NASA Lewis Research Center, NASA TM 102555 (June 1990).
25. Ganesan, P., and Smith, G.D., "An Evaluation of an Overlay Coated ODS Superalloy in High Temperature Oxidation and Burner Rig Environments," presented at NACE Conference, Corrosion 89, New Orleans, LA, Paper No. 531, pp. 1-17 (April 17-21, 1989).

26. Smith, G.D., and Fischer, J.J., "High Temperature Corrosion Resistance of Mechanically Alloyed Products in Gas Turbine Environments," presented at ASME Gas Turbine and Aeroengine Congress and Exposition, Brussels, Belgium, Paper No. 90-GT-206, pp. 1-7 (June 11-14, 1990).

27. Stoltzfus, J.M., Benz, F.J., and Homa, J., "The Pv Product Required for the Frictional Ignition of Alloys," presented at Conference on Flammability and Sensitivity of Materials in Oxygen-Enriched Atmospheres, Las Cruces, NM, Vol. 4, pp. 212-223 (April 11-13, 1989).

28. Jacobs, E.G., "Understanding the Stress-Resisting Creep and Hot Tensile Deformation in ODS Superalloys," Dissertation, Columbia University, UMI Dissertation Information Service (1990).

29. Anglin, A.E., Jr., "Transverse and Longitudinal Tensile Properties at 760 C of Several Oxide Dispersion Strengthened Nickel-Base Alloys," NASA Lewis Research Center, NASA TM-79189 (1979).

30. Gregory, J.K.; Gibeling, J.C.; and Nix, W.D., "High Temperature Deformation of Ultra-Fine-Grained Oxide Dispersion Strengthened Alloys," *Metallurgical Transactions*, Vol. 16A, No. 5, pp. 777-787 (May 1985).

31. Reppich, B.; Listl, W.; and Meyer, T., "Particle-Strengthening Mechanisms in ODS Superalloys," presented at Conference on High Temperature Alloys for Gas Turbines and Other Applications, 1986, Part II, Liege, Belgium, pp. 1023-1035 (October 6-9, 1986).

32. Whittenberger, J.D., "Elevated-Temperature Compressive Steady State Deformation and Failure in the Oxide Dispersion Strengthened Alloy MA 6000E," *Metallurgical Transactions*, Vol. 15A, No. 9, pp. 1753-1762 (September 1984).

33. Glasgow, T.K., "Longitudinal Shear Behavior of Several Oxide Dispersion Strengthened Alloys," NASA Lewis Research Center, NASA TM-78973 (August 1978).

34. Howson, T.E.; Mervyn, D.A.; and Tien, J.K., "Creep and Stress Rupture of a Mechanically Alloyed Oxide Dispersion and Precipitate Strengthened Nickel-Base Superalloy," *Metallurgical Transactions*, Vol. 11A, No. 9, pp. 1609-1616 (September 1980).

35. Arzt, E., and Singer, R.F., "The Effect of Grain Shape on Stress Rupture of the Oxide Dispersion Strengthened Superalloy Inconel MA 6000," presented at Fifth International Symposium on Superalloys, Superalloys 1984, Champion, PA, pp. 367-376 (October 7-11, 1984).

36. Zeizinger, H., and Arzt, E., "The Role of Grain Boundaries in High Temperature Creep Fracture of an Oxide Dispersion Strengthened Superalloy," *Zeitschrift fur Metallkunde*, Vol. 78, No. 12, pp. 774-781 (December 1988).

37. Arzt, E., "Creep of Dispersion Strengthened Materials: a Critical Assessment," *Res Mechanica*, Vol. 31, No. 4, pp. 399-453 (1990).

38. Timmins, R., and Arzt, E., "Diffusion Creep in a Coarse Grained ODS Superalloy Under Transverse Loading," *Scripta Metallurgica*, Vol. 22, No. 8, pp. 1353-1356 (August 1988).

39. Glasgow, T.K., "Creep Shear Behavior of the Oxide Dispersion Strengthened Superalloy MA 6000E," NASA Lewis Research Center, NASA TM-82704 (1981).

40. Shahanian, P., and Sadananda, K., "Fatigue and Creep Crack Growth Behavior of Inconel MA 6000," *High Temperature Technology*, Vol. 7, No. 3, pp. 136-144 (August 1989).

41. Stefani, J.A.; Nardone, V.C.; and Tien, J.K., "The Effect of High Frequencies on the Cyclic Creep Behavior of an ODS Superalloy," *Scripta Metallurgica*, Vol. 21, No.1, pp. 1-6 (January 1987).

42. Kim, Y.G., and Merrick, H.F., "Fatigue Properties of MA 6000E, a Gamma Prime Strengthened Superalloy," presented at AIME/ASM Fourth International Symposium on Superalloys, Superalloys 1980, Champion, PA, pp. 551-561 (September 21-25, 1980).

43. Hoffelner, W., and Singer, R.F., "High-Cycle Fatigue Properties of the ODS-Alloy MA 6000 at 850 deg C," *Metallurgical Transactions*, Vol. 16A, No. 3, pp. 393-399 (March 1985).

44. Bressers, J., and Arzt, E., "High Temperature Low Cycle Fatigue of Inconel MA 6000," presented at Conference on High Temperature Alloys for Gas Turbines and Other Applications, 1986, Part II, Liege, Belgium, pp. 1067-1080 (October 6-9, 1986).

45. Marchionni, M., Ranucci, D., and Picco, E., "Influence of Environment on High Temperature Low Cycle Failure of an Oxide Dispersion Strengthened Nickel Base Superalloy," presented at Conference on High Temperature Materials for Power Engineering, 1990, Part II, Liege, Belgium, pp. 1195-1204 (September 24-27, 1990).

46. Hynna, A.; Kuokkala, V.-T.; Lepisto, T.; Mantyla, T.; and Kettunen, P., "High Temperature Low Cycle Fatigue Properties of Superalloy MA 6000," presented at Conference on High Temperature Alloys for Gas Turbines and Other Applications, 1986, Part II, Liege, Belgium, pp. 1091-1102 (October 6-9, 1986).

47. Marchionni, M.; Ranucci, D.; and Picco, E., "High Temperature LCF of an Oxide Dispersion Strengthened Nickel Base Superalloy," presented at Conference on Low Cycle Fatigue and Elasto-Plastic Behavior of Materials, Munich, FRG, pp. 730-735 (September 7-11, 1987).

48. Elzey, D.M., and Arzt, E., "Oxide Dispersion Strengthened Superalloys: The Role of Grain Structure and Dispersion During High Temperature Low Cycle Fatigue," presented at AIME Sixth International Symposium on Superalloys, Superalloys 1988, Champion, PA, pp. 595-604 (September 18-22, 1988).
49. Elzey, D.M., and Arzt, E., "Analysis and Modeling of the Creep-Fatigue Behavior of Oxide Dispersion Strengthened Superalloys," presented at Conference on New Materials by Mechanical Alloying Techniques, Calw-Hirasu, FRG, pp. 231-239 (October 3-5, 1988).
50. Tekin, A., and Martin, J.W., "Fatigue Crack Growth Behavior of MA 6000," *Materials Science and Engineering*, Vol. 96, pp. 41-49 (December 1987).
51. Gabrielli, F., "High Temperature Fatigue and Creep Crack Growth in Nickel Base Superalloys," presented at Conference on High Temperature Alloys for Gas Turbines and Other Applications, 1986, Part II, Liege, Belgium, pp. 1639-1648 (October 6-9, 1986).
52. Sadananda, K., and Shahanian, P., "Crack Growth Behavior in Mechanically Mixed Oxide Dispersion Strengthened Alloys," presented at Conference on Failure Mechanisms in High Performance Materials, Gaithersburg, MD, pp. 87-97 (May 1-3, 1984).
53. Gabrielli, F.; Vimercati, G.; and Lupinc, V., "Environmental Effects on High Temperature Fatigue Crack Growth Behavior of Nickel Base Superalloys (Retroactive Coverage)," presented at Conference on Mechanical Behavior of Materials, V, Vol. 2, Beijing, China (June 3-6, 1987).
54. Gregory, J.K., "Superplastic Deformation in Oxide Dispersion Strengthened Nickel Base Superalloys," Dissertation, Stanford University, UMI Dissertation Information Services (1983).
55. Schroder, G.; Rydstad, H.; and Gessinger, G.H., "Improved Properties of Forged Superalloys - Results of a Better Modelling and Controlling of the Forging Process," presented at Conference on Advanced Technology of Plasticity 1987, Vol. II, Stuttgart, FRG, pp. 1073-1080 (August 24-28, 1987).
56. Grundy, E.; Precious, C.J.; and Pinder, D., "Hot Forming of Mechanically Alloyed Gas Turbine Components," *Metal Powder Reports*, Vol. 40, No. 10, pp. 565-569 (October 1985).
57. Grundy, E., "Structure and Properties of Forged ODS Nickel-Base Superalloys," presented at International Conference on PM Aerospace Materials - 87, Luzern, Switzerland, pp. 12.1-12.10 (November 2-4, 1987).
58. Moracz, D.J., "Fabrication Development for ODS-Superalloy, Air-Cooled Turbine Blades," TRW Materials and Manufacturing Technology Center, NASA CR-174650 (January 1984).
59. Hack, G.A.J., "Production, Properties and Fabrication of Mechanically Alloyed Dispersion Strengthened Alloys," presented at Conference on Advanced Materials and Processing Techniques for Structural Applications, Paris, France, pp. 309-325 (September 7-9, 1987).
60. Moore, T.J., and Glasgow, T.K., "Diffusion Welding of MA 6000 and a Conventional Nickel-Base Superalloy," *Welding Journal*, Vol. 64, No. 8, pp. 219s-226s (August 1985).
61. Verpoort, C.; Nazmy, M.; and Jongenburger, C.P., "HIP-Diffusion Bonding of ODS MA 6000," *Metal Powder Reports*, Vol. 43, No. 2, pp. 107-113 (February 1988).
62. Howson, T.E.; Cosandey, F.; and Tien, J.K., "Creep Deformation and Rupture of Oxide Dispersion Strengthened Inconel MA 754 and MC 6000E," presented at AIME/ASM Fourth International Symposium on Superalloys, Superalloys 1980, Champion, PA, pp. 563-573 (September 21-25, 1980).
63. Been, R.C., "Oxide Dispersion Strengthened Superalloys for Long-Term Service," presented at Third International Conference on Creep and Fracture of Engineering Materials and Structures, Wales, U.K., pp. 319-329 (April 5-10, 1987).

This page is blank.